

KINETICS OF SULFUR: EXPERIMENTAL STUDY OF THE REACTION OF ATOMIC
SULFUR WITH ACETYLENE AND THEORETICAL STUDY OF THE
CN + SO POTENTIAL ENERGY SURFACE

Sean A. Ayling, B.S.

Thesis Prepared for the Degree of
MASTER OF SCIENCE

UNIVERSITY OF NORTH TEXAS

May 2013

APPROVED:

Paul Marshall, Major Professor
Martin Schwartz, Committee Member
William E. Acree, Jr., Chair of the
Department of Chemistry
Mark Wardell, Dean of the Toulouse
Graduate School

Ayling, Sean A. *Kinetics of Sulfur: Experimental Study of the Reaction of Atomic Sulfur with Acetylene and Theoretical Study of the CN + SO Potential Energy Surface*. Master of Science (Chemistry – Physical Chemistry), May 2013, 84 pp., 6 tables, 17 figures, reference list, 50 titles.

The kinetics of the reaction of atomic sulfur with acetylene ($S(^3P) + C_2H_2$) were investigated experimentally via the flash photolysis resonance fluorescence method, and the theoretical potential energy surface for the reaction $CN + SO$ was modeled via the density functional and configuration interaction computational methods. Sulfur is of interest in modern chemistry due to its relevance in combustion and atmospheric chemistry, in the Claus process, in soot and diamond-film formation and in astrochemistry. Experimental conditions ranged from 295 – 1015 K and 10 – 400 Torr of argon. Pressure-dependence was shown at all experimental temperatures. The room temperature high-pressure limit second order rate constant was $(2.10 \pm 0.08) \times 10^{-13} \text{ cm}^3 \text{ molecule}^{-1} \text{ s}^{-1}$. The Arrhenius plot of the high-pressure limit rate constants gave an E_a of $(11.34 \pm 0.03) \text{ kJ mol}^{-1}$ and a pre-exponential factor of $(2.14 \pm 0.19) \times 10^{-11} \text{ cm}^3 \text{ molecule}^{-1} \text{ s}^{-1}$. $S(^3P) + C_2H_2$ is likely an adduct forming reaction due to pressure-dependence (also supported by a statistical mechanics analysis) which involves intersystem crossing. The potential energy surface for $CN + SO$ was calculated at the B3LYP/6-311G(d) level and refined at the QCISD/6-311G(d) level. The PES was compared to that of the analogous reaction $CN + O_2$. Notable energetically favorable products are $NCS + O$, $CO + NS$, and $CS + NO$. The completed PES will ultimately be modeled at the CCSD(T) level (extrapolated to infinite basis set limit) for theoretical reaction rate analysis (RRKM).

Copyright 2013

by

Sean Ayling

ACKNOWLEDGEMENTS

I am hugely grateful to my major professor, Dr. Paul Marshall, for the opportunity and privilege to pursue a master's degree as part of his research group. His passion for physical chemistry and kinetics inspired me to pursue this particular subject as an undergraduate student and to continue to study in this field as a focus during graduate school. His expert knowledge and mentorship have guided my approach to scientific study throughout, and I am certain the benefit of his experience that I have gained will be invaluable to me as I soon begin a career in the chemical sciences.

In addition, I must thank the members of the Marshall research group, especially Dr. Yide Gao and Kristopher Thompson for their advice, instruction and assistance with the practical use of the research apparatus, as well as the computational modeling software.

I would like to thank the Department of Chemistry at the University of North Texas and the Robert A. Welch Foundation for financial support. I would also like to thank the Center for Advanced Scientific Computing and Modeling at the University of North Texas (funded in part by the National Science Foundation with Grant CHE-0741936) for computational resources.

TABLE OF CONTENTS

	Page
ACKNOWLEDGEMENTS	iii
LIST OF FIGURES.....	vi
1. INTRODUCTION.....	1
1.1 References	4
2. EXPERIMENTAL METHOD	6
2.1 Background	6
2.2 Gas Preparation	7
2.3 Reactor and Detection	13
2.4 Analysis	20
2.5 Results.....	28
2.6 Previous Experimental Studies.....	32
2.7 Previous Theoretical Studies	33
2.8 References	42
3. THEORETICAL MODELING	45
3.1 Introduction.....	45
3.2 Ab Initio Methods.....	46
3.3 Procedure	49
3.4 Potential Energy Surface.....	50
3.5 References	58
4. CONCLUSIONS.....	60
4.1 Experiment Conclusions.....	60

4.2 Theory Conclusions	61
APPENDIX A – FLOW CONTROLLER CALIBRATION	63
APPENDIX B – S + C ₂ H ₂ KINETICS DATA	66
APPENDIX C – S + C ₂ H ₂ ADDUCT DATA USED FOR STATISTICAL MECHANICS CALCULATIONS	71
APPENDIX D – CN + SO GEOMETRIES, ENERGIES AND FREQUENCIES.....	74
REFERENCE LIST.....	81

LIST OF FIGURES

	Page
Figure 2.1 Flow controller calibration.....	13
Figure 2.2 Reactor schematic	15
Figure 2.3 Fluorescence signal decay.....	22
Figure 2.4 Pseudo first order rate constant versus $[C_2H_2]$	23
Figure 2.5 Zero residence time extrapolations at 1015 K.....	26
Figure 2.6 Pressure dependence curves.....	30
Figure 2.7 Low-pressure limit third-order rate constant plot	31
Figure 2.8 High-pressure limit second-order rate constant plot.....	32
Figure 2.9 $S(3P) + C_2H_2$ and $S(1D) + C_2H_2$ potential energy surfaces	35
Figure 2.10 Intersystem crossing potential energy surface	35
Figure 2.11 Adduct stability	40
Figure 2.12 Adduct structures	41
Figure 3.1 $CN + SO$ doublet potential energy surface (QCISD)	51
Figure 3.2 $CN + SO$ minima and transition states	52
Figure 3.3 $CN + SO$ minima and transition states	53
Figure 3.4 $CN + SO$ minima and transition states	54
Figure 3.5 $CN + SO$ quartet minima energy levels (B3LYP)	58

CHAPTER 1

INTRODUCTION

The chemistry of sulfur is of potential importance in several areas of modern scientific interest, yet quantitative kinetics and reaction dynamics data are lacking for many of the likely elementary processes in which it is involved. Currently, sulfur is notable due to its influence on combustion and atmospheric chemistry, its behavior in the Claus desulfurization process, its interaction with diamond deposition processes and its presence in compounds observed in astrochemistry. Presented here are two kinetics-focused studies of reactions involving sulfur, each with the goal of understanding more about the chemistry of this element at a fundamental level, particularly with regard to combustion. The two studies utilize experiment and theory, respectively, to investigate this chemistry.

As a result of their biological origins, fossil hydrocarbon fuels typically also contain the elements sulfur, nitrogen and oxygen. Sulfur has been observed to affect, whether directly or indirectly, the chemical processes that occur within a combustion environment, and with sulfur being commonly present in the fuel itself, the elementary reactions of sulfur with hydrocarbons and other species typically found in a combustion environment are of significant interest.

Nitrogen oxides (NO_x) are a direct product of combustion due to the nitrogen present in fuels as well as in the atmosphere. Known mechanisms for the formation of NO_x include the high-temperature driven thermal (Zeldovich) mechanism,¹ which is primarily reactions of N and O atoms:





and the prompt (Fenimore) mechanism,² which involves reactions of nitrogen and carbon species in the fuel. The key step is the initial formation of HCN (equation 1.4).



Alternatively:



NH species can then react to produce nitrogen which can in turn react via equation 1.2 or 1.3 to generate NO, or NH species can react with oxygen and generate NO.



Once in the atmosphere, NO_x compounds can participate in photo-catalyzed reactions with compounds normally found in the atmosphere, producing what are referred to as secondary pollutants.³

The presence of sulfur has been shown to affect the rate of production of NO_x compounds in a flame.⁴ Depending on the conditions, sulfur has variously been shown to increase or inhibit NO_x production, but the mechanism by which it achieves these effects is unknown. Conditions known to be relevant include the amount of sulfur, the ratio of sulfur to nitrogen, and whether the flame is fuel-rich.^{5, 6}

The reaction of sulfur with acetylene has been described as a reaction of high interest within the context of the Claus industrial process because it could lead to CS₂

during the combustion of H₂S (equation 1.15).^{7, 8} Some proposed mechanisms for this process include:



The Claus process recovers elemental sulfur from the H₂S found in natural gas or in the hydrocarbon gas byproduct of crude oil refinement:



Another issue of concern due to the presence of sulfur in fossil fuels is that sulfur content has been observed to correlate with soot emission. Riley et al.⁹ found that emission of hazardous polyaromatic hydrocarbons from combustion of coal increased with sulfur content, and Morawska et al.¹⁰ collected data which suggests that increased sulfur content in diesel fuel significantly increases the rate of production of nanoparticles from engines.

Interestingly, in addition to soot sulfur is also implicated in influencing mechanisms that produce another form of carbon: diamond-like carbon films. Understanding the factors affecting the formation and properties of diamond-like films is highly valuable for materials scientists, as these films can be used to coat surfaces, giving them advantageous properties similar to the properties of diamond. In the creation of diamond-like films, when acetylene was used as the carbon precursor, the

presence of sulfur was shown to affect the physical properties of the diamond as the sulfur acts as a doping agent.¹¹ More kinetically relevant, formation of the sulfur-containing CS radical from H₂S is described as a key step in the reaction pathway for sulfur doping of diamond.¹²

Lastly, sulfur as well as organo-sulfur compounds have been detected in the interstellar medium as well as in cometary comae.¹³ However, under these conditions the energy available to drive reactions and the collision rate for molecules are generally very low, although the temperature in cometary comae can rise to 300 K or greater near perihelion.¹⁴

1.1 References

- (1) Zeldovich, Y. B. *Doklady Akademii Nauk SSSR, Seriya A* **1946**, 51, 217.
- (2) Fenimore, C. P. *Symp. (Int.) Combust., [Proc.], 13th*, Schenectady, NY, 1971; pp 373-380.
- (3) Finlayson-Pitts, B. J.; Pitts, Jr., J. N. *Atmospheric Chemistry*; Wiley: Chichester, 1986.
- (4) Ziehn, T.; Tomlin, A. S. *Int. J. Chem. Kinet.* **2008**, 40, 742.
- (5) Wendt, J. O. L.; Morcomb, J. T.; Corley, T. L. *17th Symp. (Int.) Combust.* **1979**, 17, 671.
- (6) Wendt, J. O. L.; Wootan, E. C.; Corley, T. L. *Combust. Flame* **1984**, 58, 144.
- (7) Gargurevich, I. A. *Ind. Eng. Chem. Res.* **2005**, 44, 7706.
- (8) McGrath, W. D.; Morrow, T.; Dempster, D. N. *Chem. Commun.* **1967**, No. 11, 516.

- (9) Liu, K.; Han, W.; Pan, W.-P.; Riley, J. T. *J. Hazard. Mater.* **2001**, *B84*, 175.
- (10) Ristovski, Z. D.; Jayaratne, E. R.; Lim, M.; Ayoko, G. A.; Morawska, L. *Environ. Sci. Technol.* **2006**, *40*, 1314.
- (11) Moolsradoo, N.; Watanabe, S. *Diamond Relat. Mater.* **2010**, *19*, 525.
- (12) Haubner, R.; Sommer, D. *Diamond Relat. Mater.* **2003**, *12*, 298.
- (13) Dello Russo, N.; DiSanti, M. A.; Mumma, M. J.; Magee-Sauer, K.; Rettig, T. W. *Icarus* **1998**, *135*, 377.
- (14) Benkhoff, J.; Boice, D. C. *Planet. Space Sci.* **1996**, *44*, 665.

CHAPTER 2

EXPERIMENTAL METHOD

2.1 Background

Flash photolysis is a highly useful and versatile technique for studying the rates of elementary reactions. A set of these reactions often represents the underlying physical mechanism of a chemical reaction, and as such, precise study of elementary reactions is the key to truly understanding the chemistry at work in a variety of processes. The advantage of the flash photolysis technique over flow techniques is the relative lack of mixing time and pressure limitations. Additionally, there are fewer complications due to reactor wall-catalyzed reactions, as the reaction is both initiated and monitored in the free space at the center of the reactor.¹ Development of the technique by Ronald Norrish and George Porter in 1949 jointly earned them the Nobel Prize for Chemistry in 1967.

Flash photolysis begins with the introduction of reactant gas mixtures of known concentration into a reactor which is held at a fixed temperature and pressure. Although the gases are initially inert, high-intensity light in the ultraviolet or visible range is directed into the reactor, rapidly creating an excited or radical species via irradiation of one of the reactant gases, referred to as the precursor. The concentration of this newly-created, reactive species can be monitored as it subsequently reacts, and this provides the data necessary to quantify the kinetics of the elementary reaction taking place. The pulse of photolytic light is generated by a lamp or laser adjacent to the reactor apparatus and must be brief, relative to the time-scale of the reaction, for the flash photolysis technique to produce results. The monochromatic, coherent, intense

light of a laser makes it ideal for photolysis.² Because the light source is central in flash photolysis, engineering advances in both optics and laser technology have improved the sophistication of the technique in the time since its initial development.

Once initially produced by flash photolysis, the concentration of the short-lived reactant must be monitored as it dissipates (due to the reaction and other processes) to provide the necessary kinetics data. There are multiple methods for detecting the concentration as it rapidly decreases. In this case, the reaction process is monitored by the resonance fluorescence (RF) technique. Resonance fluorescence was first used in this way by Braun and Lenzi³ in 1967 and is primarily used for observing atomic species rather than molecular species due to the characteristic and relatively narrow electronic transitions of atomic species. The technique works by excitation of one of the reactant species via light of a specific energy that the species will in turn emit as fluorescence. The intensity of the fluorescent light emitted is directly proportional to the concentration of that species and, with a precise detector, can thus be used as a proxy for monitoring the concentration in real-time. The light which causes the excitation is generated by a microwave flow lamp and the detection of the resulting fluorescence is achieved with a photomultiplier tube, a highly sensitive photon detector, which provides counts of photons to a desktop computer via a multichannel scaler.

2.2 Gas Preparation

The experiment takes place wholly in the gas phase. All gas mixtures, both for the reactants and for the microwave flow lamp source, are prepared in the laboratory vacuum line apparatus. The vacuum line is made from glass and includes storage

bulbs and cold traps for the storage and manipulation of gases. The apparatus is connected to both a mechanical pump and a diffusion pump allowing creation of a vacuum on the order of 10^{-3} Torr inside the line, and it is held at vacuum whenever possible to prevent contaminants accumulating in the interior. In the present case, the three gas mixtures were each introduced into the system through a different method. Prior to any manipulation of gases, the line is evacuated to the maximum possible vacuum.

Preparation of a hydrogen sulfide (H_2S) gas mixture began with introduction of high purity H_2S gas into the system from a storage cylinder (99.5%, MG Industries). Due to the high pressure in the cylinder, care had to be taken to avoid damage to the vacuum line. Once the cylinder was connected via tubing to a closed external valve on the line, the cylinder valve was opened, filling the connective tubing with H_2S gas. The cylinder valve was then closed securely and the vacuum line valve was opened to allow the fixed volume of gas in the tubing to flow into the system. If necessary, this procedure could be repeated to increase the amount of pure H_2S being introduced. The gas was then condensed into a cold trap surrounded by a Dewar flask containing a liquid nitrogen bath at 77 K. Once the H_2S had solidified, the external valve was closed, allowing the stock cylinder to be removed. Contaminant gases with low boiling points were removed by freeze-pump-thaw cycles, exposing the frozen sample to vacuum at each cycle, and the pure H_2S gas was then stored in the trap for later use in creating H_2S /argon mixture. During any manipulation or introduction of gases the pressure in the active section of the line was monitored by a pressure transducer (MKS Instruments

Type 622) connected to a digital readout. The pressure transducer has a potential range of up to 1000 Torr and an accuracy of 0.15-0.25% from the reading.

CS₂ is a liquid at room temperature (b.p. ~319 K) and so the method for introducing this compound to the system was different from that of H₂S. In this case, a glass trap was cleaned and filled with a small volume of stock liquid CS₂ (99%, Sigma Aldrich). Because CS₂ has a high vapor pressure (360.9 Torr at 25 °C)⁴ and is toxic, this procedure was carried out inside a fume hood. In addition, the glass trap was at least partially submerged in a liquid nitrogen bath inside a Dewar flask at all times. The low temperature of the liquid nitrogen bath solidifies the introduced sample and prevents the escape of CS₂ vapor. The trap was then connected directly to the vacuum line, remaining in the liquid nitrogen bath until after the connection was sealed. Once secure, the CS₂ was then purified using the same freeze-pump-thaw cycles as described for H₂S and stored in the trap so that the vapor can be used to create a CS₂/argon gas mixture.

Acetylene (C₂H₂) was introduced into the vacuum line in a similar procedure to that used for the H₂S. However, the C₂H₂ (Big Three Industries) intended for welding is not sufficiently pure for research application. High boiling point contaminants, especially acetone (C₃H₆O), must be removed from the sample. Because gaseous C₂H₂ is unstable under high pressure, potentially polymerizing with explosive force, it is stored dissolved in liquid acetone within the storage cylinder. The drop in pressure as the cylinder valve is opened causes degasification of the solution, thus providing the C₂H₂ gas. After being released gradually into the vacuum line via connective tubing (as in the H₂S procedure), the impure cylinder C₂H₂ was initially condensed into a trap submerged

in a liquid nitrogen bath. A slurry bath of liquid nitrogen and heptane at 182 K was then used on a second trap, allowing selective freezing of the acetone impurity (vapor pressure 0.0245 Torr at -91 °C)⁴ once the pure liquid nitrogen bath was removed from the first trap. The liquid nitrogen bath was then put in place again on the first trap, freezing the still largely gaseous C₂H₂ (vapor pressure 446 Torr at -91 °C)⁴ and separating it from the acetone. The trap containing solid C₂H₂ was sealed and the separated impurities (principally acetone) were allowed to evaporate from the second trap and be completely removed from the line via the vacuum exhaust. Any remaining impurities frozen with the C₂H₂ were then removed from the sample with a freeze-pump-thaw cycle, in the same way as the purification of the H₂S sample, leaving pure C₂H₂ for creation of C₂H₂/argon reactant mixtures.

The gas mixtures were each created from the respective pure samples and a large proportion of research-grade argon gas (99.9999%, Air Liquide). The procedure for creating a mixture began with placing a liquid nitrogen bath (within a Dewar flask) onto the trap containing the pure compound and placing the sample under high vacuum once it had been frozen. The vacuum was then closed off and the liquid nitrogen bath removed. As the frozen sample was warmed by the ambient temperature, the connected capacitance manometer was used to monitor the release of a fixed amount of gas into one of the empty storage bulbs. These bulbs were held at moderate vacuum overnight and then placed at high vacuum immediately prior to the mixing procedure. The partial pressure released into the storage bulb was typically 10-50 Torr and determined the resulting concentration (the desired concentration) as the gas was mixed with argon to a total pressure of approximately 1000 Torr. The mixture could be

evacuated to a lower pressure and further diluted with argon to provide a range of smaller concentrations without sacrificing precision. Because the reactor pressure affects the concentration of the reactants, the reactant mixtures were progressively diluted as the reactor pressure was raised between successive experiments.

From the storage bulbs, these mixtures were then simultaneously released into a separate rear section of the vacuum line, allowing them to mix before entering the reactor through a single connecting tube from that section. The difference in pressure between the reactor chamber and the higher pressure in the storage bulbs drives the flow of gases to the reactor. As such, the pressure in the storage bulbs must be higher than the operating pressure of the reactor for the apparatus to function. Because the total flow of gas into the reactor was approximately constant during each experiment, the pressure inside the reactor was controlled by adjusting the reactor exhaust valve. The rate of flow for each individual gas source determined the final concentration of the two reactant gases within the reactor, and this rate was set by four individual mass flow controllers (MKS Instruments Type 1159B). The mass flow controllers have an inlet port, an outlet port and a mass flow sensor to monitor the rate of gas flow. One controller provides Ar buffer gas directly to the reactor arms, while the remaining three controllers are connected to the rear section of the vacuum line and control the flow of the two reactant mixtures as well as the primary source of inert Ar bath gas. In the flow controllers, each flow rate is measured as proportional to the voltage required to maintain a constant temperature transfer through the gas between two sensors (where higher flow rates contribute greater cooling).

The mass flow controllers must be calibrated periodically. Typically this is done prior to undertaking each new project. A flow controller is calibrated by determining how the actual flow, measured by a Teledyne Hastings-Raydist bubble meter (HBM-1-A), compares to the flow setting displayed on the controller. The relationship is verified to be proportional, and a series of measurements allows for calculation of the scaling factor. The flow controller is connected directly to the bubble meter, and the displacement of a soap bubble film through the graduated cylinder is timed, providing a measure of flow in units of volume per time. Because the bubble meter is calibrated for the manufacturer's standard conditions, the measurement must be converted from laboratory conditions to the manufacturer's standard conditions via equation 2.1

$$\text{Standard Flow} = (V / t) \times (P / P_s) \times (T_s / T) \quad (2.1)$$

where V is the displaced volume in cm^3 , t is the time for displacement in minutes, P is the laboratory pressure in torr, P_s is the standard pressure (760 Torr), T_s is the standard temperature (293 K) and T is the laboratory temperature in kelvin. This leads to a calculation of the standard flow in units of standard cubic centimeters per minute (sccm). For each flow controller, five values of the actual flow rate, each an average of five measurements by the bubble meter, are plotted versus the flow rate setting displayed on the flow controller. The equation of the linear fitting of this graph provides the formula to convert displayed flow to actual flow throughout the course of the experiment.

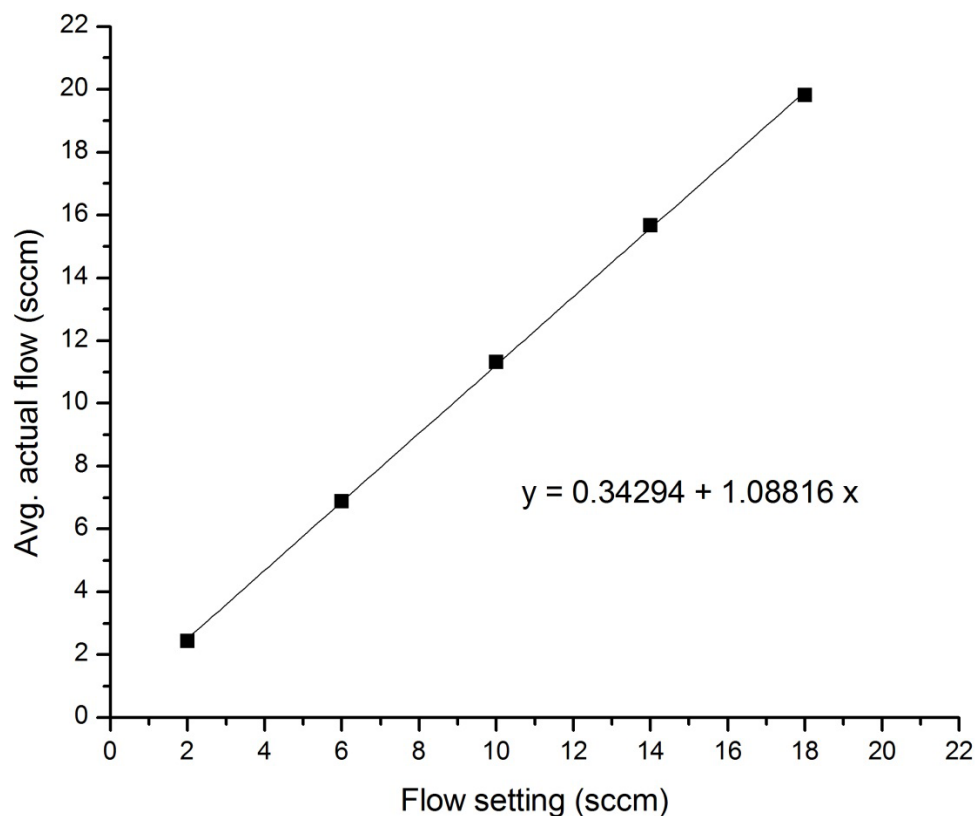


Figure 2.1 Calibration plot for flow controller #1. Data collected by Kristopher Thompson.⁵

2.3 Reactor and Detection

The reactor apparatus is constructed from stainless steel tubes, each with an interior diameter of 2.2 cm, arranged to be mutually perpendicular, as in Figure 2.2. The reaction zone is formed by the intersection of the tubes and has a volume of about 8 cm³, and the six tube “arms” of the reactor extend 11 cm from this zone. Because it is necessary to control the temperature in the reaction zone, the inner 4 cm of each arm is wrapped with nichrome resistance wire which has been threaded through ceramic beads. A thermocouple (Omega Type K) outside the reactor provides a temperature value which can be set, via a temperature controller (Omega CN 3910 K C/S), to

maintain a stable temperature. The reactor is thermally insulated by a cubic box, 20 cm on each side, constructed of 2.5 cm thick alumina boards (Zircar Products ZAL-50). This construction allows an experimental temperature range from room temperature to over 1100 K.

The end of each reactor arm extends outside the insulation and is water-cooled by wrapped copper tubing in order to protect attached optics and other fittings from the potentially high temperatures of the reaction zone. The copper jackets are connected in series and water continuously runs through them during operation of the reactor. Any time a fitting is removed and refitted to the end of a reactor arm, the seal must be tested by confirming that the reactor chamber can hold a vacuum. This is necessary because any atmospheric gases, especially oxygen, which are allowed to leak into the reactor, may participate in the reactor chemistry. This could introduce significant error into any kinetics data collected.

Each of the six reactor arms has a function. Two arms are used for the transport of the gas mixtures to and from the reactor, and the remaining four are fitted with windows or lenses. In the latter case, each of the four arms also has an inlet fixed between the window or lens and the reaction zone. These inlets are connected directly to the single mass flow controller which provides the buffer Ar gas. Placement of the inlets as described allows the flow of pure Ar to act as a buffer, protecting the optics at the end of each arm from contamination by reactant mixtures which flow through the center of the reactor.

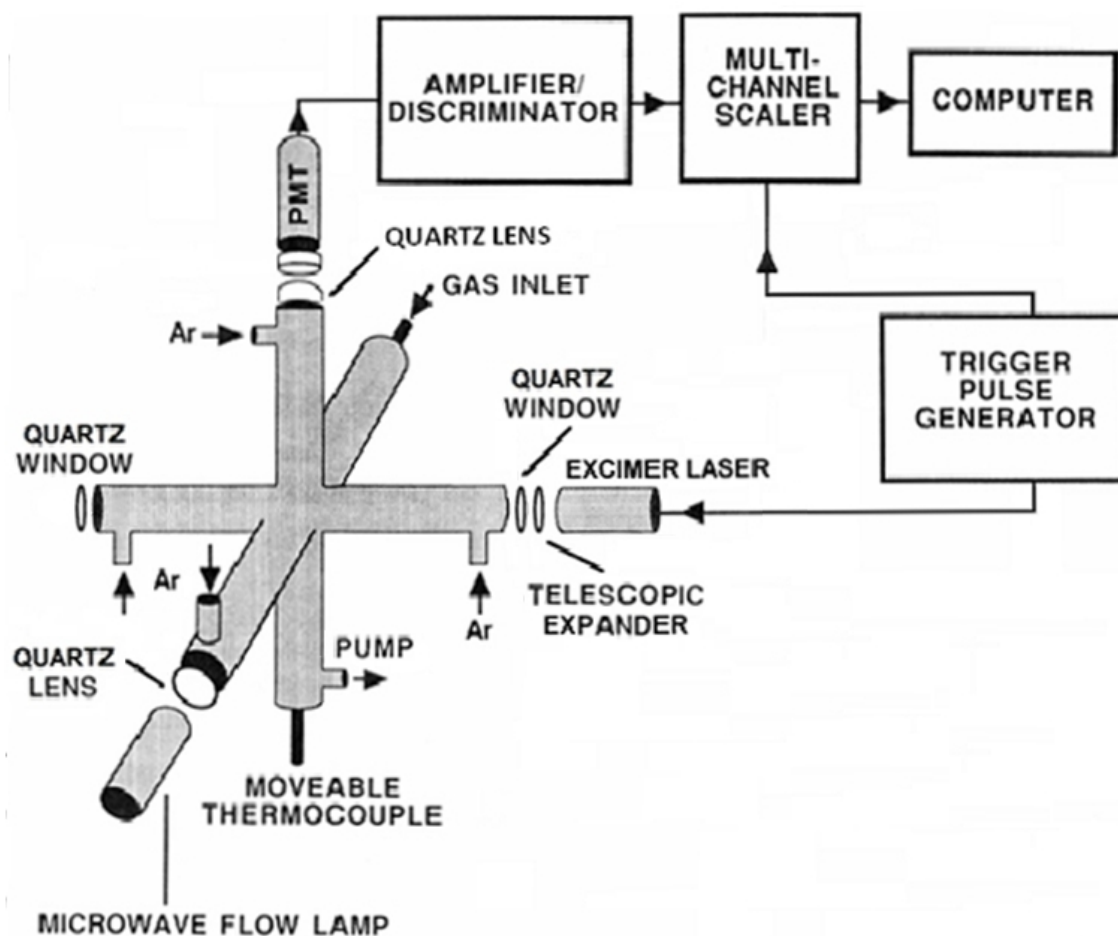


Figure 2.2. Schematic diagram of the reactor apparatus as configured for this experiment

Of the two reactor arms used for gas transport, one is used for the inflow of gas from the rear section of the vacuum line and the other, connected through a liquid nitrogen cold trap to a mechanical pump, is used for the exhaust. The end of each of these arms is fitted with tubing to allow the transport of the gas mixture to and from the reactor. The exhaust arm also functions as a fitting for a sheathed thermocouple (Omega Type K). This thermocouple is used to measure the temperature at the center of the reaction zone and is retractable so that it can be moved aside during an

experiment. The thermocouple sheath protects against damage but does not shield against radiative heat transfer, leading to a systematic error in the temperature measurements.⁶ This was corrected when analyzing the experimental data. Previous experiments to determine corrections for the error also recommended an effective uncertainty (confidence 1σ) of $\pm 2\%$ for the corrected temperature to account for possible errors in the correction procedure and thermocouple calibration.⁷

Two opposing reactor arms are fitted with windows for the excimer laser light. Each of these is fitted with a quartz window angled to allow the optimal transmission of the laser. As a safety precaution, the angle of the window is rotated such that the quartz window faces downward, causing laser light reflected from the surface of the quartz to be primarily directed away from researchers' eyes. The excimer laser (MPB PSX-100) must be aligned such that the emitted light is directed through a telescopic expander which widens the beam from a cross sectional area of 2×2 mm to 7×8 mm before it passes through the first quartz window, into the center of the reaction zone and on through the opposite window. The laser is filled with F_2 0.19%, Ar 5.0%, neon balance (Spectra Gases) and outputs light at a wavelength of 193 nm. This laser gas must be refilled periodically for the laser to output sufficient energy. During this experiment, it was typically necessary to refill the laser at least once each working week. The energy of the laser light was measured prior to running an experiment and could be lowered by placing metal mesh filters in the path of the beam. The energy of the light was measured by a pyroelectric joulemeter (Molelectron J25LP) both before and after traveling through the reactor. Both measurements are necessary to calculate the scaling factor needed to determine the energy of the laser as it passes through the

reaction zone. After taking these initial energy measurements, the face of the window opposite the laser entry window was obstructed for safety. Knowledge of the scaling factor makes it only necessary to measure the energy of the laser light before it enters the reactor.

The energy of the laser light as it passes through the reaction zone determines the initial concentration of the reactive species generated by the laser pulse. In this case the reactive species is atomic sulfur and its precursor is CS₂. Photolysis of CS₂ at 193 nm creates CS and S species via dissociation from an excited state.^{8, 9}



The branching ratio S(³P):S(¹D) was found to be 1.6 ± 0.3.¹⁰ The quenching rate constant for relaxation of S(¹D) is 1.4 × 10⁻¹¹ cm³ molecule⁻¹ s⁻¹,¹¹ meaning a lifetime for the excited state of less than 1 μs with the 10¹⁷ molecule cm⁻³ or greater Argon concentration present. This lifetime is several orders of magnitude less than the time scale for the kinetic decays being monitored, which means that the initial presence of excited state sulfur will have a negligible effect on the experimental data for the reaction rate.

The value for the initial concentration of sulfur, [S]₀, generated by photolysis is not necessary to study the kinetics of interest, but the relative value is important to consider (see section 2.4 for discussion). The value for [S]₀ can be calculated from the absorption properties of CS₂ using equations based on the Beer-Lambert Law⁸

$$I_0 = \frac{\lambda c}{h} \times \frac{F \times 0.83}{A} \quad (2.5)$$

$$I_t = I_0 e^{-\sigma [CS_2] l} \quad (2.6)$$

$$[S]_0 = I_0 - I_t \quad (2.7)$$

where λ is the wavelength of the laser pulse (193 nm), F is the flash energy of the laser pulse in Joules, A is the area of the pulse (0.6 cm^2), 0.83 is a constant factor to provide the energy of the laser pulse in the reaction zone after having passed through the first reactor window, σ is the absorption cross section of CS_2 ($2.72 \times 10^{-16} \text{ cm}^2$),¹² and l is the path length through the sample (1 cm is chosen to provide a working volume of 1 cm^3). Equation 2.5 multiplies the inverse of the energy of a photon (i.e. photons J^{-1}) of 193 nm wavelength with the energy of the laser pulse per unit area to provide a calculated intensity, I_0 , in units of photons cm^{-2} . This value is scaled via the Beer-Lambert law in equation 2.6, providing a calculated transmitted intensity, I_t . The difference between these two values is due to absorption by CS_2 , and therefore, provides a value for the initial concentration of sulfur.

The microwave flow lamp which provides the resonance fluorescence radiation is fitted to a reactor arm oriented perpendicular to the excimer laser. The resonance radiation is produced by 0.01% H_2S diluted with argon flowing through a microwave discharge (2.45 GHz) operated at approximately 30 Watts. It is important to adjust the microwave discharge such that the feedback power is minimal (less than 2 Watts), in order to prevent damage to the microwave generator. The H_2S/Ar gas mixture flows directly from a storage bulb, through the lamp and is removed via an exhaust tube attached to a rotary pump (Welch 1402). Prior to the start of the experiment, the flow of gas from the bulb is adjusted by a fine valve to produce approximately 150 mTorr pressure inside the lamp chamber and the microwave discharge is initiated with a Tesla

coil. Quartz optics, fitted between the lamp and the reactor, direct the resonance radiation (181 nm) to the reaction zone and cut off any light with a wavelength below 160 nm. Because H_2S is used to produce the resonance fluorescence for sulfur, hydrogen fluorescent light (122 nm) is also generated. Use of quartz optics prevents this additional radiation from entering the reactor.

Resonance fluorescence from the transient atomic sulfur within the reaction zone is detected by a solar-blind PMT (Hamamatsu R212) which is fitted perpendicular to both the laser and the microwave flow lamp to minimize background signal from those sources. The PMT acts as a photon detector, multiplying the photoelectric effect of incident photons to produce a viable voltage signal, and is powered by a high voltage supply at 2.490 kV (Bertran Model 215). This signal is sent to a multi-channel scaler (EG&G Ortec ACE) via a preamplifier/discriminator (MIT, Inc. F-100T). The preamplifier/discriminator is necessary to achieve the optimal signal-to-noise ratio, and it is calibrated to a threshold which filters out weak signals generated by thermally emitted electrons inside the PMT. The multi-channel scaler produces a plot of photon count as a function of time, cumulative over approximately 100-8,000 laser pulses, which describes the exponential decay of fluorescence intensity following a laser pulse. Precise timing of each pulse is controlled by a digital delay/pulse generator. The laser pulse is triggered after the multi-channel scaler so that a brief segment of the background signal can be measured prior to the fluorescence decay.

2.4 Analysis

As a second-order bimolecular process, the reaction between C₂H₂ and sulfur depends on the concentration of both species. The rate of the reaction, expressed in terms of the loss of transient sulfur atoms due to the primary reaction is



$$\text{Rate} = d[\text{S}] / dt = -k_1 [\text{S}] [\text{C}_2\text{H}_2] \quad (2.9)$$

where the rate constant k_1 represents the rate constant for the second order reaction.

In addition to the expected chemistry, sulfur atoms can be lost from the reaction zone by physical diffusion and, potentially, by secondary reactions with photolysis fragments, with the photolytic precursor CS₂ or with products of the primary reaction.



$$d[\text{S}] / dt = -k' [\text{S}] \quad (2.11)$$

The total rate of sulfur loss is then a combination of equations 2.9 and 2.11.

$$d[\text{S}] / dt = -k_1 [\text{S}] [\text{C}_2\text{H}_2] - k' [\text{S}] \quad (2.12)$$

This second order rate expression is simplified by flooding the reactor with a much higher concentration of one of the reactants. In this experiment the concentration of sulfur is much smaller than that of C₂H₂.

$$[\text{S}] \ll [\text{C}_2\text{H}_2] \quad (2.13)$$

The mixture concentrations and flow rates are set such that the concentration of sulfur in the reactor is at least two orders of magnitude smaller than the concentration of C₂H₂. In this case, there was typically a difference of three orders of magnitude. Under these conditions, the concentration of C₂H₂ is effectively constant for the duration of the reaction, thus creating a system with approximately first order kinetics. The value for

the C_2H_2 concentration, treated as a constant, is combined with k' and the second order rate constant k_1 to describe the rate constant for this system, the pseudo-first order rate constant k_{ps1} . Substituting this into equation 2.12 gives the first order rate expression.

$$d[S] / dt = -k_{ps1} [S] \quad (2.14)$$

where

$$k_{ps1} = k_1 [C_2H_2] + k' \quad (2.15)$$

Because the fluorescence signal intensity is proportional to the concentration of the transient atomic sulfur species, the values for the pseudo first order rate constant k_{ps1} and its uncertainty were determined directly from the exponential decay of the intensity over time. An example of such a decay is shown in Figure 2.3. The signal intensity can be expressed through the proportionality as

$$[S] = [S]_0 e^{-k_{ps1}t} \quad (2.16)$$

$$I \propto [S] \quad (2.17)$$

$$I = [S]_0 C e^{-k_{ps1}t} + B \quad (2.18)$$

where $[S]_0$ is the initial sulfur concentration, C is the constant of proportionality and B accounts for the signal resulting from constant background radiation. A non-linear, least-squares fit of the exponential decay to equation 2.18 yields k_{ps1} and its uncertainty.^{13, 14}

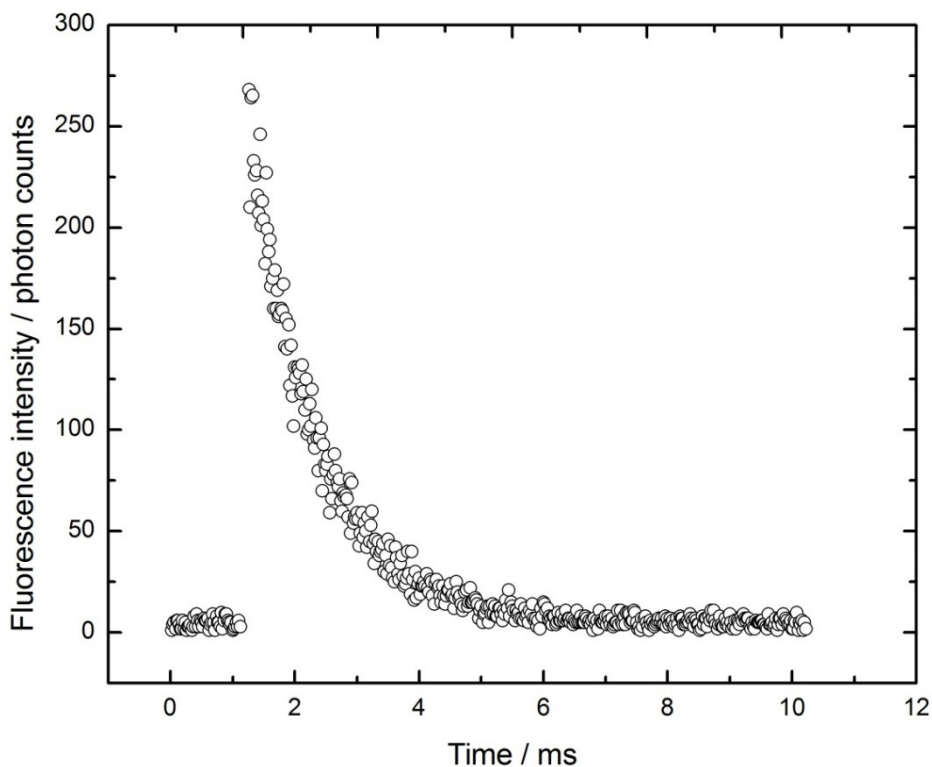


Figure 2.3. Exponential decay of fluorescence signal intensity following a laser pulse.

The concentration of C_2H_2 is calculated by partial pressures, flow proportions and the ideal gas law ($R = 1.04 \times 10^{-19} \text{ cm}^3 \text{ Torr molecule}^{-1} \text{ K}^{-1}$).

$$n / V = [C_2H_2] = P_{C_2H_2} / RT \quad (2.19)$$

$$P_{C_2H_2} = (P_{C_2H_2, \text{bulb}} / P_{\text{tot, bulb}}) \times (\text{Flow}_{C_2H_2} / \text{Flow}_{\text{tot}}) \times P_{\text{tot, system}} \quad (2.20)$$

$$a_{\text{bulb}} = P_{C_2H_2, \text{bulb}} / P_{\text{tot, bulb}} \quad (2.21)$$

$$[C_2H_2] = a_{\text{bulb}} \times (\text{Flow}_{C_2H_2} / \text{Flow}_{\text{tot}}) \times P_{\text{tot, system}} / RT \quad (2.22)$$

The uncertainty in the concentration of C_2H_2 is calculated by propagation of the uncertainties for the terms in equation 2.22.

$$\sigma_{[C_2H_2]} = [C_2H_2] \times \left\{ \left(\frac{\sigma_{P_{\text{tot}}}}{P_{\text{tot}}} \right)^2 + \left(\frac{\sigma_{F_{C_2H_2}}}{F_{C_2H_2}} \right)^2 + \left(\frac{\sigma_{F_{\text{tot}}}}{F_{\text{tot}}} \right)^2 + \left(\frac{\sigma_{a_{\text{bulb}}}}{a_{\text{bulb}}} \right)^2 + \left(\frac{\sigma_T}{T} \right)^2 \right\}^{1/2} \quad (2.23)$$

The terms in equation 2.23 relate to the total pressure, the flow of acetylene, the total flow, the dilution ratio of the acetylene mixture, and the temperature, respectively.

For an experiment, a value for k_{ps1} was determined at five different concentrations of acetylene, the lowest in every case being zero, with the reaction zone at constant temperature and pressure. This data allows construction of a plot of k_{ps1} versus $[C_2H_2]$ as in the example shown in Figure 2.4. According to equation 2.15, such a plot should be linear with an intercept of k' and a slope of k_1 , the second order rate constant. In practice, a weighted linear least-square fitting provided the value for the slope.

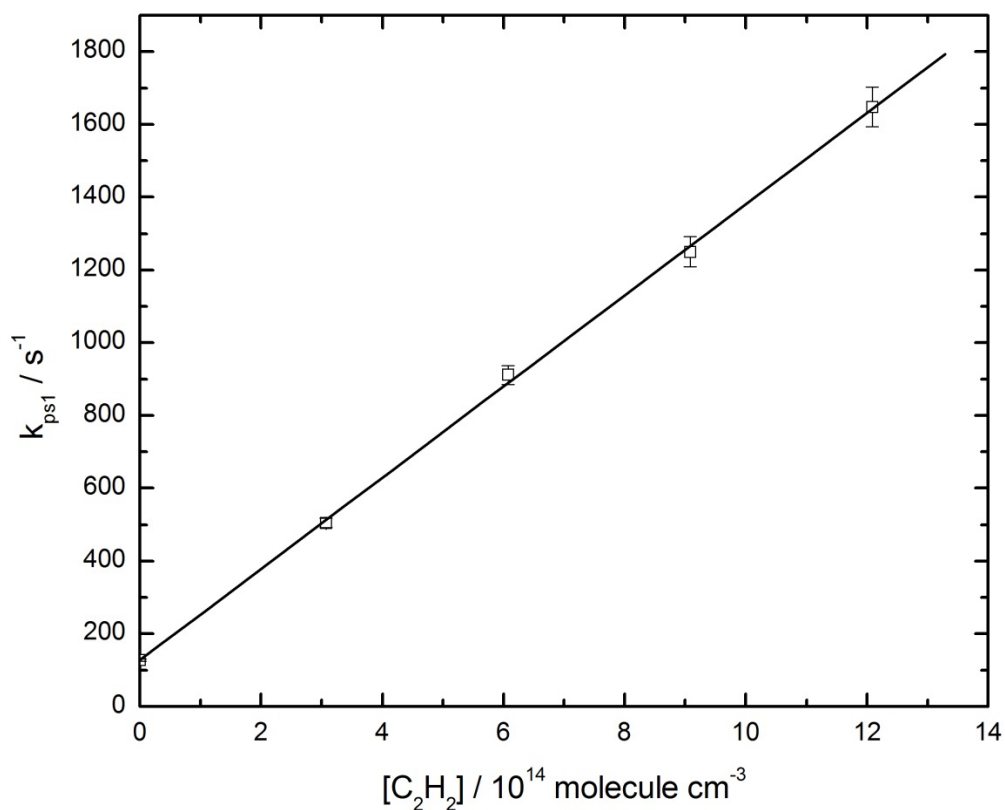


Figure 2.4. Pseudo first order rate constant versus acetylene concentration at approximately 1015 K and 100 Torr. The value of k_{ps1} for the second point of this plot was obtained from the decay in Figure 2.3.

During the experiment, several parameters must be considered in order for the determined second order rate constants to be accurate. At each experimental temperature, the variable parameters of residence time (τ_{res}), photolysis energy (F), photolysis precursor concentration ($[\text{CS}_2]$) and initial sulfur radical concentration ($[\text{S}]_0$) are adjusted to determine suitable working values. That is, to determine values which minimize the effects of secondary processes and maintain bimolecular kinetics such that the C_2H_2 concentration is the only variable controlling the rate during each set of measurements.

The additional complexity of photolysis and photoexcitation of C_2H_2 itself must also be considered, although effects are expected to be minimal with the chosen conditions. The absorption cross section of C_2H_2 at 193 nm is only on the order of $10^{-19} \text{ cm}^2 \text{ molecule}^{-1}$ ($(1.34 \pm 0.05) \times 10^{-19} \text{ cm}^2 \text{ molecule}^{-1}$ at 193.3 nm) as measured by Okabe and Seki,¹⁵ whereas the absorption cross section for CS_2 at 193 nm is on the order of $10^{-16} \text{ cm}^2 \text{ molecule}^{-1}$ ($2.72 \times 10^{-16} \text{ cm}^2 \text{ molecule}^{-1}$ at 193.44 nm) according to Xu and Joens.¹²

Though temperature is held constant for each set of measurements, the temperature may still potentially cause errors in the measured rate constant either by thermal degradation of the reactants or by favoring reactions between the reactant and the radical precursor as the gas mixtures are being transported to the reaction zone. To rule out these effects, the average gas residence time within the reactor (τ_{res}) can be varied to determine a range where there is no significant change in the rate of sulfur decay. The main reason to vary τ_{res} is to check for any thermal decomposition of the reaction mixture after it has entered the hot reactor but before photochemistry is

initiated by the laser. Varying τ_{res} can also check whether the gases have had adequate mixing time prior to entering the reaction zone. Because higher pressures necessitate a higher value of τ_{res} , the high end of the range must cover the residence time calculated for the maximum desired pressures. In the present case, it was not possible to eliminate residence time effects at the experimental temperature of ~ 1015 K.

Extrapolation to a theoretical zero-residence time was utilized to determine the best value for the second order rate constant, as shown in Figure 2.5.

As with the gas residence time, the photolysis energy (F) produced by the excimer laser must be varied to find a range where there is negligible change in the sulfur decay rate. Varying the photolysis energy can rule out secondary chemistry which might occur with photolysis fragments or reaction products, and which would otherwise contribute to the loss of additional sulfur in the reaction zone. Variation of the CS_2 concentration ($[\text{CS}_2]$) can also rule out the influence of secondary reactions. As the photolysis energy and $[\text{CS}_2]$ both determine the initial sulfur radical concentration $[\text{S}]_0$, mindful variation of those parameters additionally accounts for the $[\text{S}]_0$ variable.

The remaining variables of pressure and temperature were varied systematically, and the rate constant was determined at several constant pressures for each experimental temperature. Whether the rate varies with pressure or not can provide insight into the kinetic mechanisms. Pressure dependence, as is present here, is often due to the formation of an adduct during the reaction. The Lindemann theory of unimolecular reactions¹⁶ describes such a mechanism as





where the reactants A and B come together to form an energetic complex which can either dissociate due to the excess energy released by formation of the new A-B bond or be stabilized by collision with a bath gas M to form an adduct.

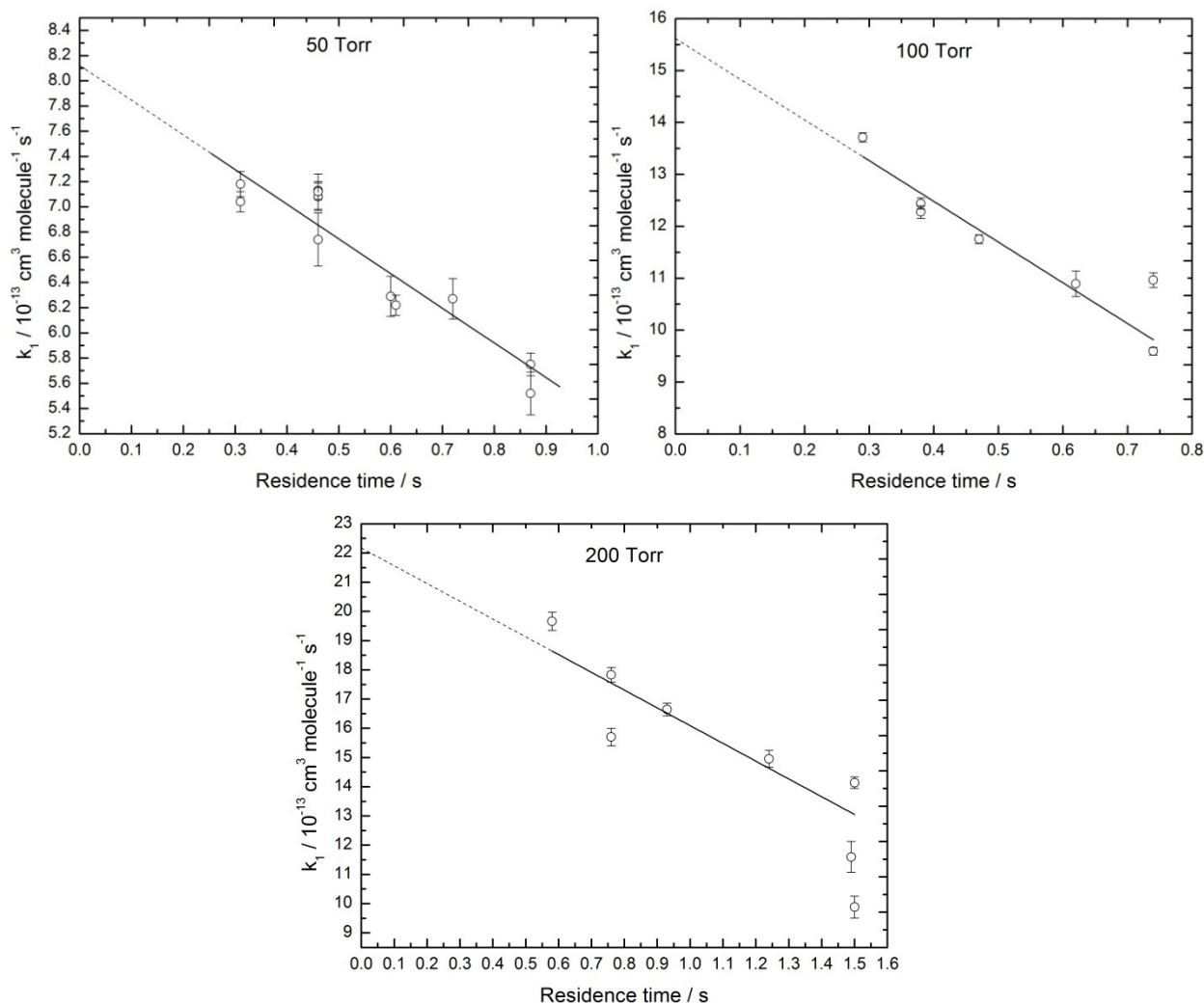


Figure 2.5. Extrapolations from data to theoretical zero residence time at 1015 K.

Stabilization is favored with an increase in bath gas concentration due to the resulting increase in the rate of collision between species. As the bath gas concentration

increases with pressure, the rate constant is expected to increase with pressure if the reaction is adduct-forming.

The rate constant for formation of the adduct is referred to as the recombination rate constant, k_{rec} , and it can be described in terms of the low- and high-pressure rate constants, and $[M]$, the bath gas concentration.

$$k_{\text{rec}} = \left(\frac{k_0[M]}{1+k_0[M]/k_\infty} \right) \quad (2.27)$$

Troe's empirical formalism¹⁷ provides an empirical scaling factor F for k_{rec} which improves agreement between the kinetic theory and experiment

$$F = F_{\text{cent}}^{\left\{ 1 + [\log_{10}(k_0[M]/k_\infty)] / (0.75 - 1.27 \log_{10} F_{\text{cent}}) \right\}^2 }^{-1} \quad (2.28)$$

where F_{cent} is the broadening factor. In this case, a value of 0.6 is used for the broadening factor, appropriate when the reactants have two rotational degrees of freedom.¹⁸ This leads to the complete empirical expression for the recombination rate constant

$$k_{\text{rec}} = \left(\frac{k_0[M]}{1+k_0[M]/k_\infty} \right) \times F_{\text{cent}}^{\left\{ 1 + [\log_{10}(k_0[M]/k_\infty)] / (0.75 - 1.27 \log_{10} F_{\text{cent}}) \right\}^2 }^{-1} \quad (2.29)$$

Svante Arrhenius used empirical observation to develop an equation which describes the relationship between the rate of a chemical reaction and the temperature. It was published in 1889 and is now known as the Arrhenius equation:¹⁹

$$k = A e^{-E_a/RT} \quad (2.30)$$

In the Arrhenius equation, A is the pre-exponential factor, E_a is the activation energy of the reaction, R is the gas constant and T is the temperature. By taking the natural logarithm of both sides of equation 2.30, a linear equation is produced

$$\ln k = -(E_a/R) \times (1/T) + \ln A \quad (2.31)$$

where, on a plot of $\ln k$ vs $1/T$, the slope of the straight line is $-E_a/R$ and the intercept is $\ln A$. Most often the slope of the line is negative, which indicates a positive activation energy. This energy is described as a barrier which must be overcome for the reaction to proceed. In the case of a positive slope for the line described by equation 2.31, the activation energy would be negative, indicating a barrierless reaction.²

2.5 Results

A total of 94 measurements, listed in Table 2.2, were taken across the range of experimental conditions for which the rate constant was determined to be unaffected by secondary chemistry or other effects separate from the kinetics of interest. The rate was dependent on the argon bath concentration at all experimental temperatures (see Figure 2.6). The curves shown on the graphs are weighted, least-squares fittings to the equation for the recombination rate constant, including Troe's scaling factor (equation 2.29). The parameters for these fittings are the low- and high-pressure rate constants, k_0 and k_{inf} . Plots of the resulting low-pressure and high-pressure limit rate constant values (see Table 2.1) are shown in Figures 2.7 and 2.8.

Looking closely, we can see in Figure 2.6 that the fall-off pressure increases with temperature. The fall-off pressure is the pressure at which k_{rec} is half the value of k_{inf} , in the region where the rate is not adequately described by either the low- or high-pressure rate expressions, and it represents the point at which the reverse of the recombination equilibrium is balanced with the rate of stabilization. Temperature

dependence is expected by unimolecular rate theory because (from equations 2.24 - 2.26) the reaction relies on stabilization of the activated complex by the bath gas:



As the temperature increases, the efficiency of the collisional stabilization decreases.

Therefore, a greater concentration of M is required to compete with the reverse reaction and achieve the same rate of product formation.

Note that the value for the low-pressure limit rate constant at 1015 K has relatively small error because the slope of the curve is approximately linear close to zero and the fitting interpolates between the given data and the origin intercept, while the value for the high-pressure limit rate constant has relatively large error due to the limitations of the extrapolation to an asymptote far beyond the range of pressures that were viable for the apparatus (less than 1 atm). Consequently, the high-pressure limit rate constant at 1015 K has very little bearing on the weighted fitting of the Arrhenius plot. The Arrhenius expression derived from the high-pressure limit experimental data (Figure 2.8) was

$$k = ((2.14 \pm 0.19) \times 10^{-11} \text{ cm}^3 \text{ molecule}^{-1} \text{ s}^{-1}) e^{-((11.34 \pm 0.03) \text{ kJ mol}^{-1}) / RT}$$

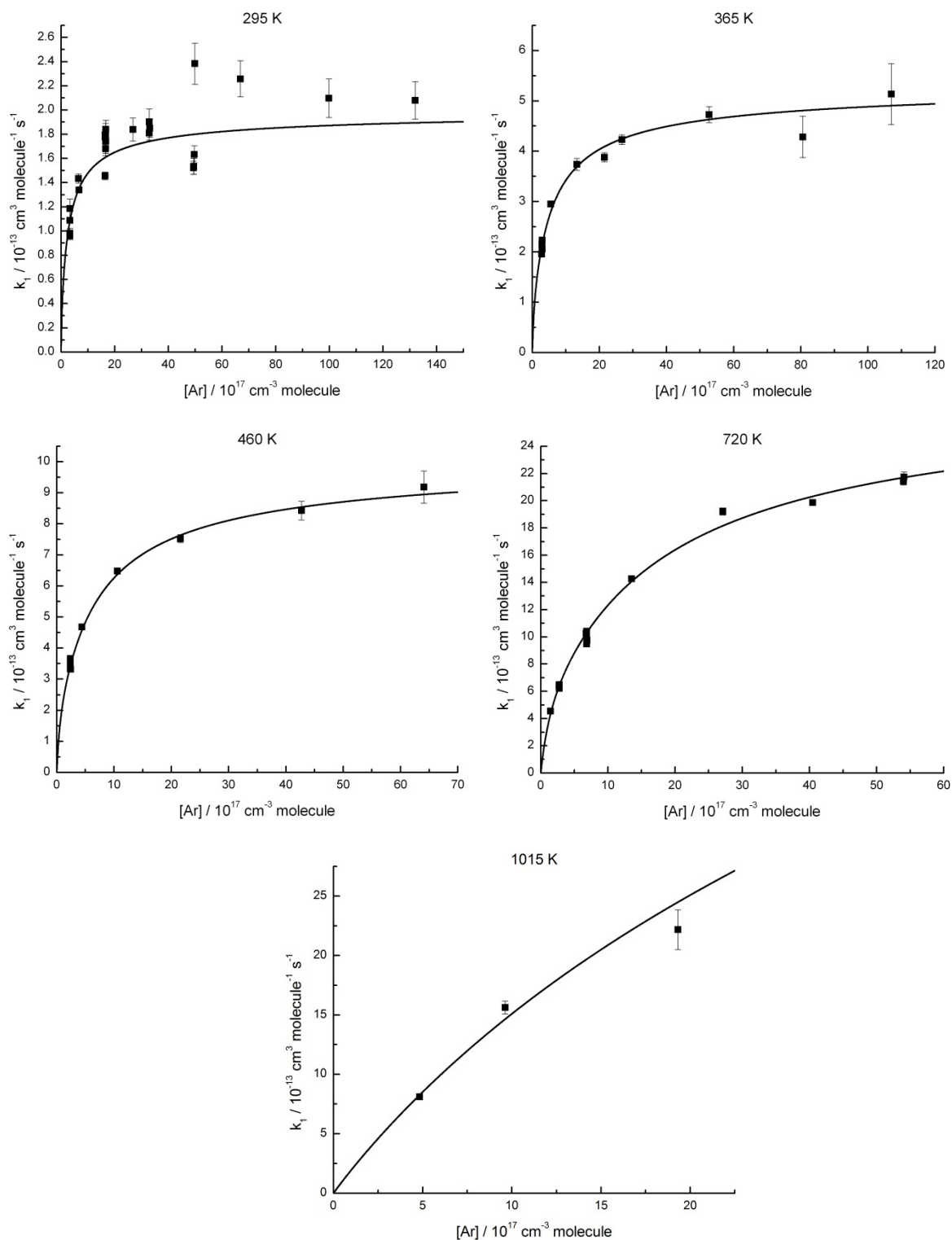


Figure 2.6. Pressure dependence of the second-order rate constant (confidence 1σ) at each experimental temperature. Troe fit curves ($F_{\text{cent}} = 0.6$) are superimposed.

Temperature (K)	Low-pressure limit rate constant ($k_0 / \text{cm}^6 \text{ molecule}^{-2} \text{ s}^{-1}$)	High-pressure limit rate constant ($k_{\text{inf}} / \text{cm}^3 \text{ molecule}^{-1} \text{ s}^{-1}$)
295	$(2.18 \pm 0.19) \times 10^{-30}$	$(2.10 \pm 0.08) \times 10^{-13}$
365	$(3.10 \pm 0.25) \times 10^{-30}$	$(5.68 \pm 0.33) \times 10^{-13}$
460	$(5.02 \pm 0.26) \times 10^{-30}$	$(1.10 \pm 0.05) \times 10^{-12}$
720	$(5.50 \pm 0.21) \times 10^{-30}$	$(3.14 \pm 0.11) \times 10^{-12}$
1015	$(2.21 \pm 0.34) \times 10^{-30}$	$(1.98 \pm 1.41) \times 10^{-11}$

Table 2.1 Low- and high-pressure limit rate constants (confidence 1σ), at each experimental temperature, as determined by fitting to the recombination rate constant expression.

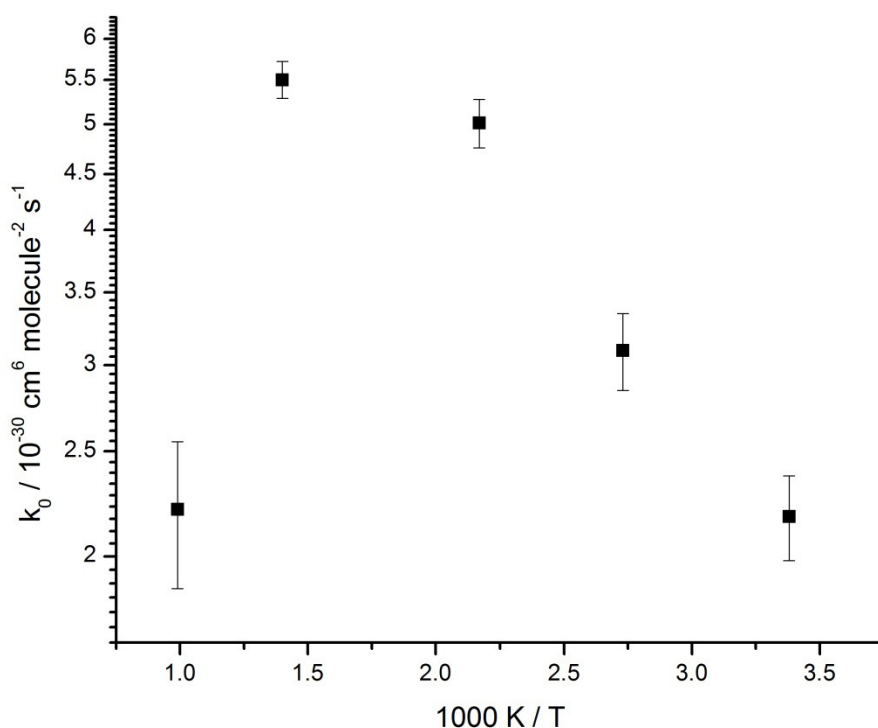


Figure 2.7. Plot of the low-pressure limit third-order rate constant (confidence 1σ)

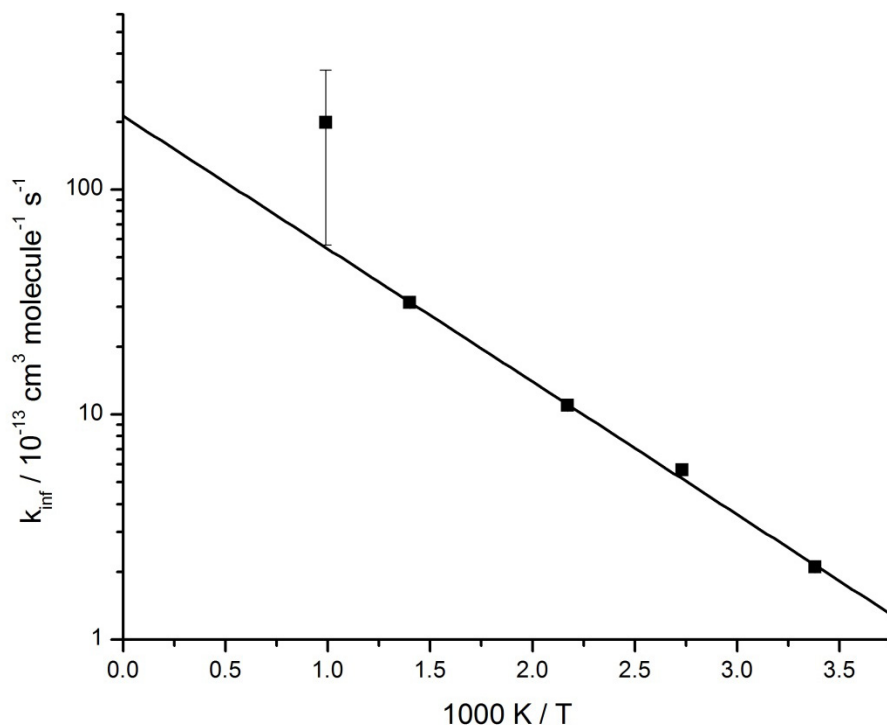


Figure 2.8. Plot of the high-pressure limit second-order rate constant (confidence 1σ)

2.6 Previous Experimental Studies

The range of temperatures and pressures used in earlier experimental studies of the reaction between acetylene and sulfur has been greatly expanded by this work. Experimental conditions for a study of the reaction by Little and Donovan were limited to room temperature and approximately 150 Torr of argon. Pressure dependence was assumed but not demonstrated. The pressure of 150 Torr was chosen in order to provide a rate constant close to the high-pressure limit.²⁰ A similar study of the reaction by Gunning et al. used a pressure of approximately 200 Torr of CO_2 and temperatures ranging from room temperature to 480 K.²¹

At room temperature, Little and Donovan found the absolute rate constant for $\text{S} (^3\text{P}) + \text{C}_2\text{H}_2$ to be $(5.0 \pm 0.5) \times 10^{-13} \text{ cm}^3 \text{ molecule}^{-1} \text{ s}^{-1}$ using flash photolysis and

vacuum UV absorption spectroscopy.²⁰ Using the same technique, Gunning et al. determined a rate constant of $(3.8 \pm 0.7) \times 10^{-13} \text{ cm}^3 \text{ molecule}^{-1} \text{ s}^{-1}$ at room temperature and an energy of activation of $\sim 13 \text{ kJ mol}^{-1}$ for the reaction.²¹

The measurements in the present investigation were taken over a temperature range of approximately 300 – 1015 K and a pressure range of approximately 10 – 400 Torr of Argon. Pressure dependence of the rate constant was observed at all experimental temperatures, as shown in Figure 2.6 of the previous section, indicating that the reaction mechanism is likely dominated by the formation of one or more adducts. These adducts must be stable even at 1015 K. Adduct formation can be inferred from pressure dependence because collisional stabilization of an intermediate species would be directly related to the rate of molecular collisions, which is itself proportional to the total pressure. The high-pressure limit rate constant was found to be $(2.1 \pm 0.1) \times 10^{-13} \text{ cm}^3 \text{ molecule}^{-1} \text{ s}^{-1}$ at room temperature, significantly lower than the values determined previously.

2.7 Previous Theoretical Studies

The reactions of ground state S (^3P) + C₂H₂ were characterized by Woon via ab initio calculations at the coupled cluster RCCSD(T) level of theory²² using the aug-cc-pV(T+d)Z and aug-cc-pV(D+d)Z basis sets.²³ It was found that the only reaction pathway on the triplet potential energy surface, that of the formation of HCCS + H products, was significantly endothermic ($\Delta H_0^\circ = +84.9 \text{ kJ mol}^{-1}$) with a barrier height of $+114 \text{ kJ mol}^{-1}$. A theoretical study by Leonori et al. explored the S (^1D) + C₂H₂ singlet potential energy surface at the W1 level of theory.²⁴ In this case, formation of HCCS +

H was found to be exothermic relative to the excited state of sulfur. Further, there were several low energy adducts along the surface. The reaction pathways of these two studies are shown, superimposed, in Figure 2.9.

Because the only feasible reaction on the triplet potential energy surface has a barrier far in excess of the observed E_a , there is likely to be an instance of intersystem crossing as the reaction proceeds from the ground state reactants. The energy barrier for this intersystem crossing was found to be approximately 10 kJ mol^{-1} .²⁵ The value of 10 kJ mol^{-1} was calculated via a relaxed scan of the potential energy surfaces for both S (^1D) and S (^3P) approaching C_2H_2 perpendicular to the C-C bonds, computed with the B3LYP/6-311G(d,p) level of theory, as shown in Figure 2.10. It should be noted that this calculated value for the barrier is close to the activation energy shown by the Arrhenius plots for the present experimental investigation as well as the experimental investigation by Gunning et al.²¹

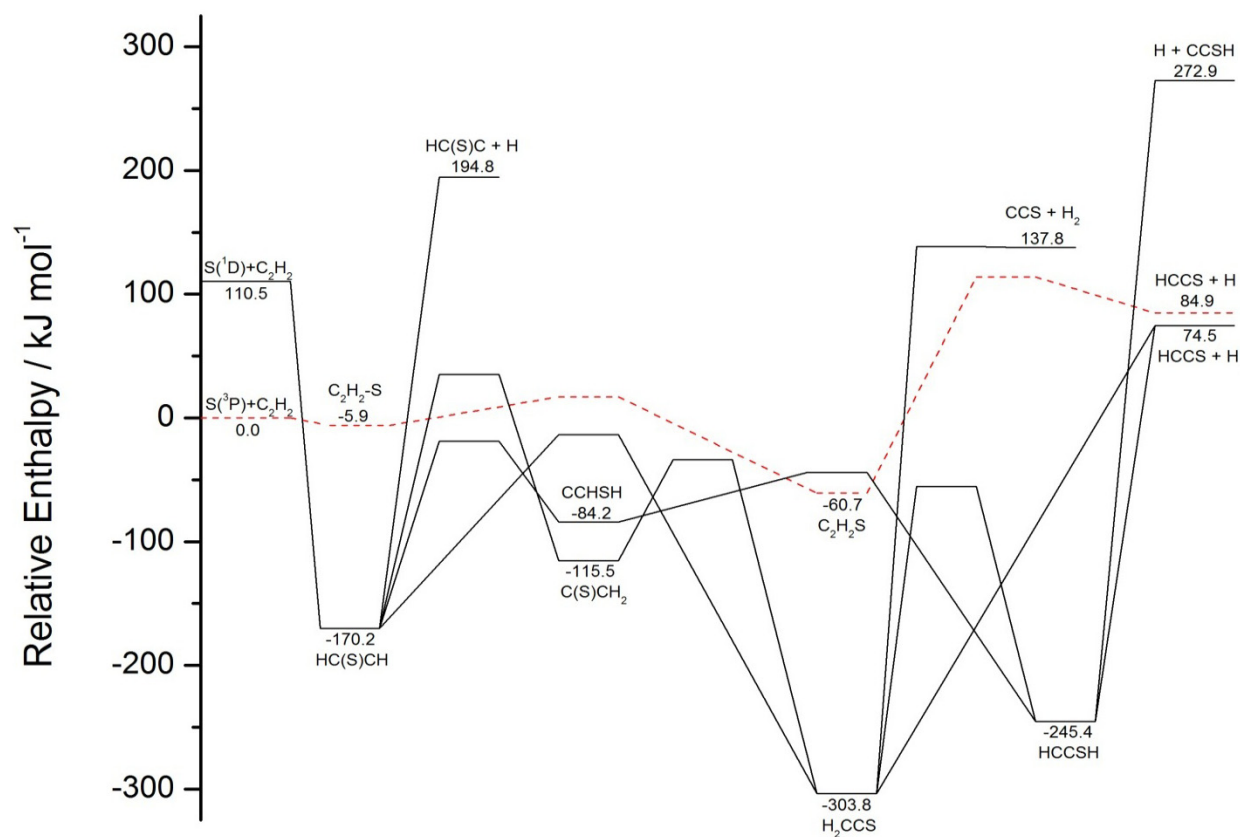


Figure 2.9. $S(^3P) + C_2H_2$ (RCCSD(T)) and $S(^1D) + C_2H_2$ (W1) potential energy surfaces.^{23, 24}

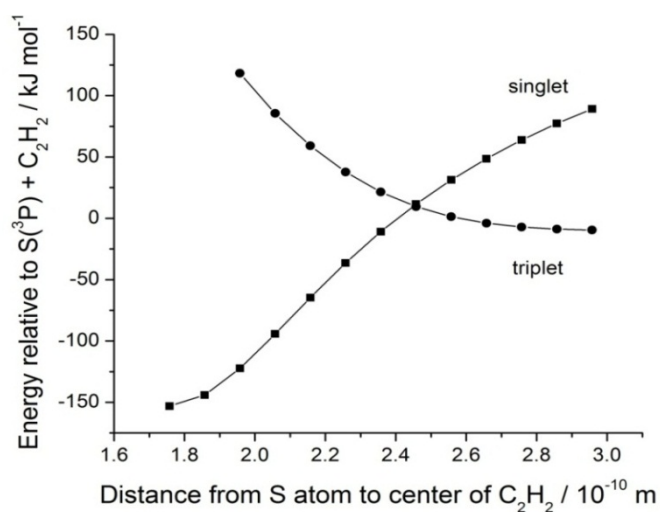


Figure 2.10. DFT (B3LYP) illustration of intersystem crossing calculated by Paul Marshall.²⁵

As discussed in the previous two sections, the present experimental investigation found pressure dependence for the second-order rate constant at all studied temperatures from 298 K to 1015 K. This implies the formation of adducts at all studied temperatures, and we can expect the theoretical potential energy surface to support this.

Statistical thermodynamics allows us to determine the concentration equilibrium constant (K_c) for the formation of each adduct from the reactants, provided the relative enthalpy of the species are known, as they are from the theoretical potential energy surface.



$$K_c = \frac{Q_{\text{adduct}}}{Q_{\text{reactants}}} e^{-\Delta H/RT} \quad (2.34)$$

where Q are the total partition functions, ΔH is the difference in enthalpy (J mol^{-1} at 0 K), R is the gas constant ($\text{J mol}^{-1} \text{K}^{-1}$) and T is the temperature (K). The partition functions for acetylene and sulfur were calculated from experimental values.²⁶ For sulfur the energies and degeneracies of the ground state atom ($J = 0, 1, 2$) were used, while for acetylene the single rotational constant as well as the vibrational frequencies and degeneracies of the ground state molecule were used. The moment of inertia, necessary for determining the total partition function of acetylene, was calculated from the rotational constant by

$$I = \frac{h}{8 \pi^2 B} \quad (2.35)$$

where I is the moment of inertia (kg m^2), h is Planck's constant ($\text{kg m}^2 \text{s}^{-1}$) and B is the rotational constant (Hz). The total partition function for the reactants was calculated by

$$Q_{\text{reactants}} = Q_{\text{sulfur}} \times Q_{\text{acetylene}} \quad (2.36)$$

The partition function for each adduct on the singlet PES was calculated from theoretical values determined by Leonori et al.²⁴ The vibrational frequencies were obtained directly from their published data, while the rotational constants (and thus, moments of inertia) were obtained from the literature B3LYP-optimized geometries via a single-point Hartree-Fock calculation. For the adduct on the triplet PES, the bond lengths were obtained from Woon's published theoretical data.²³ A B3LYP optimization was used to determine bond angles. This was followed by a single-point calculation to obtain the rotational constants. All calculations were performed via the Gaussian 03 program.²⁷

In addition to being related to the partition functions, the equilibrium constant can also be expressed by

$$K_c = \frac{[\text{adduct}]}{[\text{C}_2\text{H}_2][\text{S}]} \quad (2.37)$$

From equation 2.33 it can be seen that an adduct is produced from reactant sulfur in a 1:1 ratio. Given that $[\text{C}_2\text{H}_2]$ is effectively constant during the reaction

$$K_c = \frac{x}{[\text{C}_2\text{H}_2]([\text{S}]_0 - x)} \quad (2.38)$$

where the variable x is the concentration of adduct produced. As a rough guideline, if we declare that adduct stability is favored when more than half of the sulfur reacts to produce adduct, that is

$$x > \frac{[\text{S}]_0}{2} \quad (2.39)$$

then the criterion for adduct stability is

$$K_c > \frac{[\text{S}]_0/2}{[\text{C}_2\text{H}_2]([\text{S}]_0 - [\text{S}]_0/2)} \quad (2.40)$$

or, simplified,

$$K_c > \frac{1}{[C_2H_2]} \quad (2.41)$$

At each temperature, the value chosen for the acetylene concentration in this expression is obtained by taking the average of the maximum acetylene concentrations for all runs at that temperature and dividing by two. This provides a rough estimate of the median value for the concentration. A comparison between the resulting minimum K_c value (equation 2.41) and the calculated K_c values for each adduct (equation 2.34) at each of the five experimental temperatures can be seen in Figure 2.11, and the structure for each adduct is shown in Figure 2.12. Even at 1015 K, formation of the two most stable adducts remains favored, providing a correlation with the experimental pressure dependence of the current investigation.

At all temperatures, the six adduct species show the same stability trend. This trend follows that of the theoretical relative enthalpies on the PES, with the adduct that is most exothermic relative to the reactants being the most stable at all temperatures and vice versa. The least stable adduct (C_2H_2S), which is the only adduct on the triplet surface, does not meet the criterion for stability at any of the experimental temperatures. The varying stability of the singlet PES adducts can be at least partly attributed the potential bonding patterns for each. In the two most stable adducts, H_2CCS and $HCCSH$, there are only four sigma bonds, but the linear geometry suggests multiple pi bonds and fully-substituted carbons. The next two adducts, $HC(S)CH$ and $C(S)CH_2$, have five sigma bonds and may have a carbon-carbon pi bond, but the structures include cyclic geometry with sharp internal angles adding significant ring-strain to the system. Removal of sulfur from $HC(S)CH$ leaves acetylene, as per the PES, while the structure of $C(S)CH_2$ suggests that removing sulfur would leave vinylidene ($:C=CH_2$).

The ΔH from vinylidene to acetylene is approximately -184 kJ mol^{-1} ,²⁸ yet the ΔH between their derivatives, from C(S)CH_2 to HC(S)CH , is only $-54.7 \text{ kJ mol}^{-1}$. This difference in ΔH suggests that sulfur has a significant relative stabilizing effect on vinylidene beyond that expected by the exothermicity. The geometry of the least stable adduct on the singlet PES includes only four sigma bonds but may allow for a pi bond between the two carbons. If so, it could suggest a structure similar to vinylidene but with a thiol group substituted for one of the hydrogens. As shown by Leonori et al.,²⁴ the isomerization from this compound, CCHSH , to HCCSH is accomplished by the shifting of a hydrogen and has a barrier of $+40.2 \text{ kJ mol}^{-1}$. The analogous barrier for isomerization from vinylidene to acetylene is approximately $+11.6 \text{ kJ mol}^{-1}$,²⁸ indicating that the presence of sulfur lowers the activation energy for isomerization.

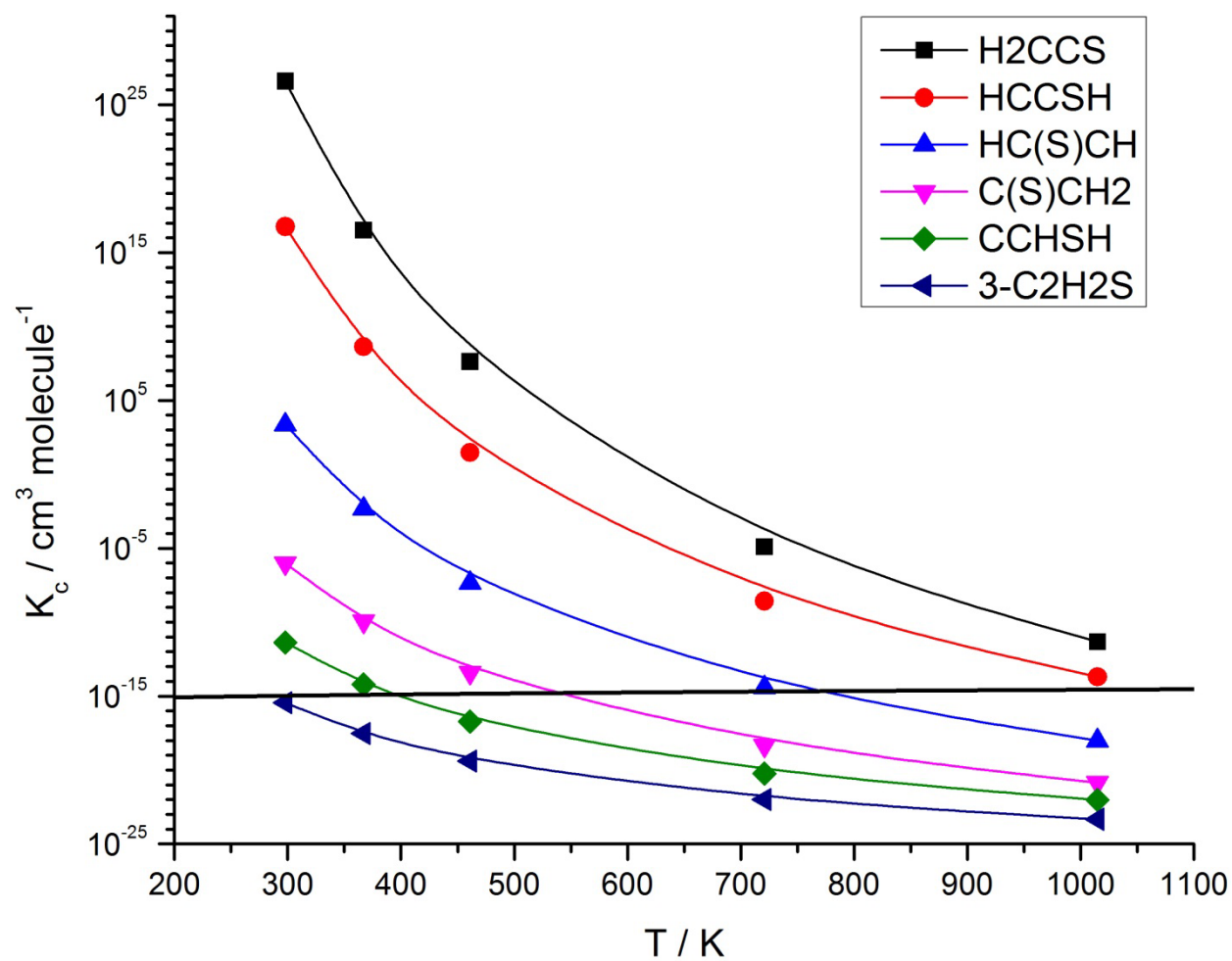


Figure 2.11. Theoretical K_c for each adduct at varying temperature. The line is the plot of the linear fit for the approximate minimum values of K_c necessary to favor adduct formation.

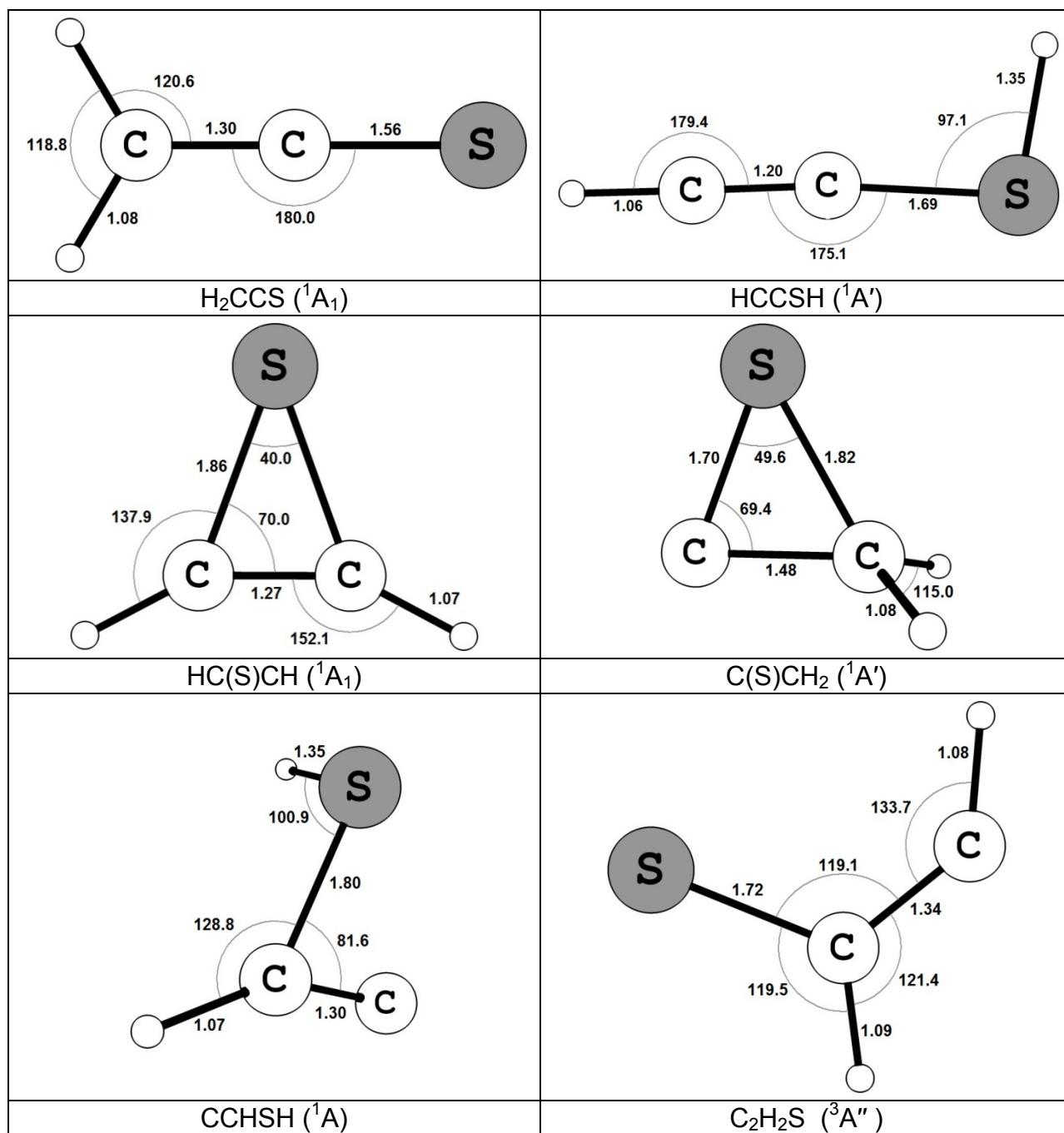


Figure 2.12. Structures of the adducts for both the S(¹D) and S(³P) potential energy surfaces, in order of stability, starting with the most stable adduct.

2.8 References

- (1) Pilling, M. J.; Seakins, P. W. *Reaction Kinetics*; Oxford Science Publications: Oxford, 1995.
- (2) Steinfeld, J. I.; Francisco, J. S.; Hase, W. L. *Chemical Kinetics and Dynamics*, 2nd ed.; Prentice hall: Upper Saddle River, 1999.
- (3) Braun, W.; Lenzi, M. *Faraday Society* **1967**, *44*, 252.
- (4) Dean, J. A., Ed. *Lange's Handbook of Chemistry*, 13th ed.; McGraw-Hill: New York, 1985.
- (5) Thompson, K. University of North Texas, Denton, TX. Personal Communication, 2013.
- (6) Fontijn, A.; Felder, W. *Reactive Intermediates in the Gas Phase*; Academic Press: New York, 1979.
- (7) Ding, L.; Marshall, P. *J. Chem. Soc. Faraday Trans.* **1993**, *89*, 419-423.
- (8) Okabe, H. *Photochemistry of Small Molecules*; Wiley: New York, 1978.
- (9) Black, G.; Jusinski, L. E. *Chem. Phys. Letters* **1986**, *124*, 90.
- (10) Dadong, X.; Jianhua, H.; Jackson, W. M. *J. Chem. Phys.* **2004**, *120*, 3051.
- (11) Black, G.; Jusinski, L. E. *J. Chem. Phys.* **1985**, *82*, 789.
- (12) Xu, H.; Joens, J. *Geophys. Res. Lett.* **1993**, *20*, 1035.
- (13) Marshall, P. *Comput. Chem.* **1987**, *11*, 219.
- (14) Marshall, P. *Comput. Chem.* **1989**, *13*, 103.
- (15) Seki, K.; Okabe, H. *J. Phys. Chem.* **1993**, *97*, 5284-5290.
- (16) Lindemann, F. A. *Trans. Faraday Soc.* **1922**, *17*, 598.
- (17) Troe, J. *J. Phys. Chem.* **1979**, *83*, 114.

- (18) Cobos, C.; Troe, J. Z. *Phys. Chem.* **2003**, 217, 1031-1044.
- (19) Arrhenius, S. Z. *Physic. Chem.* **1889**, 4, 226.
- (20) Little, D. J.; Donovan, R. J. *J. Photochem.* 1973, 1, 371-377.
- (21) van Roodselaar, A.; Safarik, I.; Strausz, O. P.; Gunning, H. E. *J. Amer. Chem. Soc.* **1978**, 100, 4068-4073.
- (22) Watts, J. D.; Gauss, J.; Bartlett, R. J. *J. Chem. Phys.* **1993**, 98, 8718.
- (23) Woon, D. *J. Phys. Chem. A* **2007**, 111, 11249-11253.
- (24) Leonori, F.; Petrucci, R.; Balucani, N.; Hickson, K.; Hamberg, M. *J. Phys. Chem. A* **2009**, 113, 4330-4339.
- (25) Marshall, P. University of North Texas, Denton, TX. Personal Communication, 2013.
- (26) Chase, M. W. *NIST JANAF Thermochemical Tables*, 4th ed.; American Institute of Physics: Woodbury, 1998.
- (27) Frisch, M. J.; Trucks, G. W.; Schlegel, H. B.; Scuseria, G. E.; Robb, M. A.; Cheeseman, J. R.; Montgomery, J. A. J.; Vreven, T.; Kudin, K. N.; Burant, J. C.; Millam, J. M.; Iyengar, S. S.; Tomasi, J.; Barone, V.; Mennucci, B.; Cossi, M.; Scalmani, G.; Rega, N.; Petersson, G. A.; Nakatsuji, H.; Hada, M.; Ehara, M.; Toyota, K.; Fukuda, R.; Hasegawa, J.; Ishida, M.; Nakajima, T.; Honda, Y.; Kitao, O.; Nakai, H.; Klene, M.; Li, X.; Knox, J. E.; Hratchian, H. P.; Cross, J. B.; Bakken, V.; Adamo, C.; Jaramillo, J.; Gomperts, R.; Stratmann, R. E.; Yazyev, O.; Austin, A. J.; Cammi, R.; Pomelli, C.; Ochterski, J. W.; Ayala, P. Y.; Morokuma, K.; Voth, G. A.; Salvado, P.; Dannenburg, J. J.; Zakrzewski, V. G.; Dapprich, S.; Daniels, A. D.; Strain, M. C.; Farkas, O.; Malick, D. K.; Rabuck, A. D.; Raghavachari, K.; Foresman, J. B.; Ortiz, J. V.; Cui, Q.; Baboul, A.

G.; Clifford, S.; Cioslowski, J.; Stefanov, B. B.; Liu, G.; Liashenko, A.; Piskorz, P.; Komaromi, I.; Martin, R. L.; Fox, D. J.; Keith, T.; A, A.-L. M.; Peng, C. Y.; Nanayakkara, A.; Challacombe, M.; Gill, P. M. W.; Johnson, B.; Chen, W.; Wong, M. W.; Gonzalez, C.; Pople, J. A. Gaussian 03, revision C.02; Gaussian, Inc. Wallingford, CT, 2004.

(28) Bowman, J. M.; Zou, S. *Chem. Phys. Lett.* **2003**, 368, 421.

CHAPTER 3

THEORETICAL MODELING

3.1 Introduction

Theoretical computational modeling of chemical reactions is of increasing importance in a variety of research fields. Available computing power for a fixed cost increases substantially each year, and new theoretical models are being developed which allow more efficient and more accurate results via their calculations. The sophisticated models typical in modern computational chemistry evaluate molecules in quantum mechanical terms using complex mathematical functions which describe the electronic structure, and development of these theoretical models is now a field of chemistry in its own right. Broadly speaking, development in this field involves improving accuracy of results while maintaining or reducing computational cost, which can currently be prohibitive for larger systems.

The benefits of theoretical studies can be appreciated both in terms of the advantages of theoretical modeling itself as well as the valuable dynamic between model and experiment. Because theoretical studies use only virtual models, investigations can be undertaken much more easily and cheaply when studying materials that would be hazardous or expensive in a physical experiment. In such cases, as well as in general practice, theoretical modeling can allow experimental studies to be targeted at promising chemistry or experimental conditions and in so doing allow much more efficient experimental work. Additionally, agreement between experiment and theory provides satisfying mutual verification of the results, while

disagreement can provoke further study, potentially leading to new insights both for the experiment and the theory.

3.2 *Ab Initio* Methods

Ab initio computational methods are those methods which use only the mathematics of relevant physical principles to calculate the energy of a system. These contrast with the semi-empirical methods which include correction factors to fit their theoretical models to experimental data. The starting point for the *ab initio* methods used in this investigation is the Hartree-Fock (HF) method, also known as the self-consistent field (SCF) method. This method determines the energy of a system by iterative application of the variational principle to an ansatz (trial wave function) consisting of a single Slater determinant. A Slater determinant is used because it intrinsically satisfies the antisymmetry requirement of the electronic wave function.

Hartree-Fock theory makes several useful approximations to limit the complexity of the calculations. Notably, there is a simplification of the interaction between electrons. As a consequence of using only one Slater determinant to define the wave function, each electron is implicitly treated as though it is moving in an average field of the other electrons. This approximation, known as a mean-field approximation, causes the energy to be necessarily higher than the exact energy, as it cannot account for the relative lowering of energy caused by electron correlation. Because the motion of electrons is in reality physically correlated by their mutual repulsion, there is a reduced probability of finding one electron located close to another. As such, electrons will tend to be spaced further apart (and thus have lower potential energy) than implied by the

mean-field approximation. In neglecting correlation, the HF method fails to account for approximately 1% of the total energy, and this energy is often important for describing chemical phenomena.¹ The two methods used in this study, density functional theory (DFT) and configuration interaction (CI), both include correlation and apply it as a correction to the HF energy. The correlation energy can be expressed simply as

$$E_{\text{corr}} = E_{\text{HF}} - E \quad (3.1)$$

where E_{HF} is the energy as calculated by Hartree-Fock theory and E is exact energy value.

Density functional theory (DFT) operates on the principle that the energy of a molecule is a function of the varying electron density, itself a function of position. The energy is thus a function-of-a-function, which is termed a functional. The specific DFT method used in this case was B3LYP which denotes a combination of the Becke three-parameter hybrid functional² and the Lee, Yang and Parr density functional theory method.³ Because DFT methods are relatively inexpensive computationally, the B3LYP method was used as a starting point for all theoretical investigations in this study.

The quadratic configuration interaction singles-doubles (QCISD) method⁴ provides improved accuracy relative to B3LYP, especially with respect to molecular geometry and vibrational frequencies. However, due to the computational cost of this method, QCISD was not used for exploration of the PES but rather as a refinement of results obtained from B3LYP optimizations. Configuration interaction is a method for improving on the Hartree-Fock energy by attempting to account for electron correlation. Hartree-Fock theory provides the best energy calculation for a single Slater determinant

so, in configuration interaction, additional Slater determinants are added. The additional determinants are constructed as excited states relative to the Hartree-Fock determinant, and the coefficients, a_i , for each determinant are calculated such that they minimize the energy (the variational principle). For singles-doubles (SD) the additional determinants consist of all possible permutations of exciting one or two electrons, as allowed by the basis set.¹

$$\Psi_{CI} = a_0 \Phi_{HF} + \sum_S a_S \Phi_S + \sum_D a_D \Phi_D \quad (3.2)$$

In addition to the method, a basis set must be defined for each theoretical calculation. The basis set represents the mathematical functions which will be used to describe the electronic structure of the system. Larger basis sets allow a more accurate mathematical model but require greater computational cost. The basis set for all final results in this theoretical investigation was 6-311G(d)⁵, although it was necessary to use smaller basis sets in some cases as an initial step. The 6-311G(d) basis set denotes a Pople-style basis set with a triple-zeta valence representation. The core orbitals are described by a single contracted Gaussian-type orbital (CGTO) function, a linear combination of six primitive Gaussian-type orbitals (PGTO). The valence orbitals are each described by three CGTO functions comprised of three, one and one PGTO, respectively. Using three CGTO functions (triple-zeta) is useful for describing the more diffuse valence orbitals because it provides additional flexibility. Additionally, a p-type and d-type polarization function is added for each atom, improving the accuracy of the calculation.

3.3 Procedure

Analysis of the ground-state reaction between the radical species CN and SO is accomplished within the framework of construction of a potential energy surface (PES) using the Gaussian 03 computational chemistry software package.⁶ Once complete, the PES can provide theoretical values for the rate constants via analysis using transition state theory (TST) or Rice, Ramsperger, Kassel and Marcus (RRKM) theory.

Construction of the PES began with all plausible arrangements of the constituent atoms of the reactant species being used as inputs for DFT optimization calculations at the B3LYP/6-311G(d) level of theory. Successful optimization of input configurations provided the geometry, energy and vibrational frequencies for each of the variety of stationary points possible in the reaction. These are placed as local minima on the PES diagram, where the vertical axis represents the energy (stated as energy relative to the summed energy of the reactants; the CN and SO radicals), and will subsequently be connected to form reaction pathways which lead from the reactants to the products.

Many of the minima are likely to be connected through energy barriers which, according to transition state theory, define intermediate, short-lived transitional configurations of the atoms. Discovery of likely transition states begins with a relaxed scan of the relevant reaction coordinate (the variable coordinate) by incrementally imposing a change in the distance or angle between various atoms in the theoretical model and then optimizing the energy with that limitation in place. The resulting graph of optimized energy as a function of the reaction coordinate can be interpreted as the plot of the lowest energy pathway between two local minima. Thus, the maximum point on the plot of the scan approximately represents the saddle-point on a two-dimensional

plot of the PES (that is, the transition state). This point is likely to be close to the optimal transition state geometry, and is used as the starting point for a subsequent transition state optimization calculation which provides the geometry, energy and vibrational frequencies of the transition state. In order to be a true transition state, the optimization should provide a structure with exactly one imaginary vibrational frequency. Additionally, care must be taken that the transition states do connect the correct pairs of minima on the PES. Critical observation of the graphical representation of the imaginary frequency can provide a visual cue of the likely minima, and is typically sufficient to confirm that the PES is being constructed correctly. If there is doubt, an intrinsic reaction coordinate (IRC) calculation can be performed which will attempt to map the full reaction coordinate associated with a given transition state. Some paths between stationary points on the PES, whether representing endothermic or exothermic processes, have no peak. This indicates a path between two minima which has no transition state, and which therefore has no energy requirement other than the energy change between the two points. Such a path is referred to as being barrierless. A barrierless process can be confirmed by the absence of any local maxima on a detailed relaxed scan of the reaction coordinate.

3.4 Potential Energy Surface

As the potential energy surface is developed, the molecular geometries obtained from the DFT calculations for both stationary and saddle points were used as inputs for new optimizations at the QCISD/6-311G(d) level. The results of these optimizations represent a more accurate PES, as shown in Figure 3.1 below.

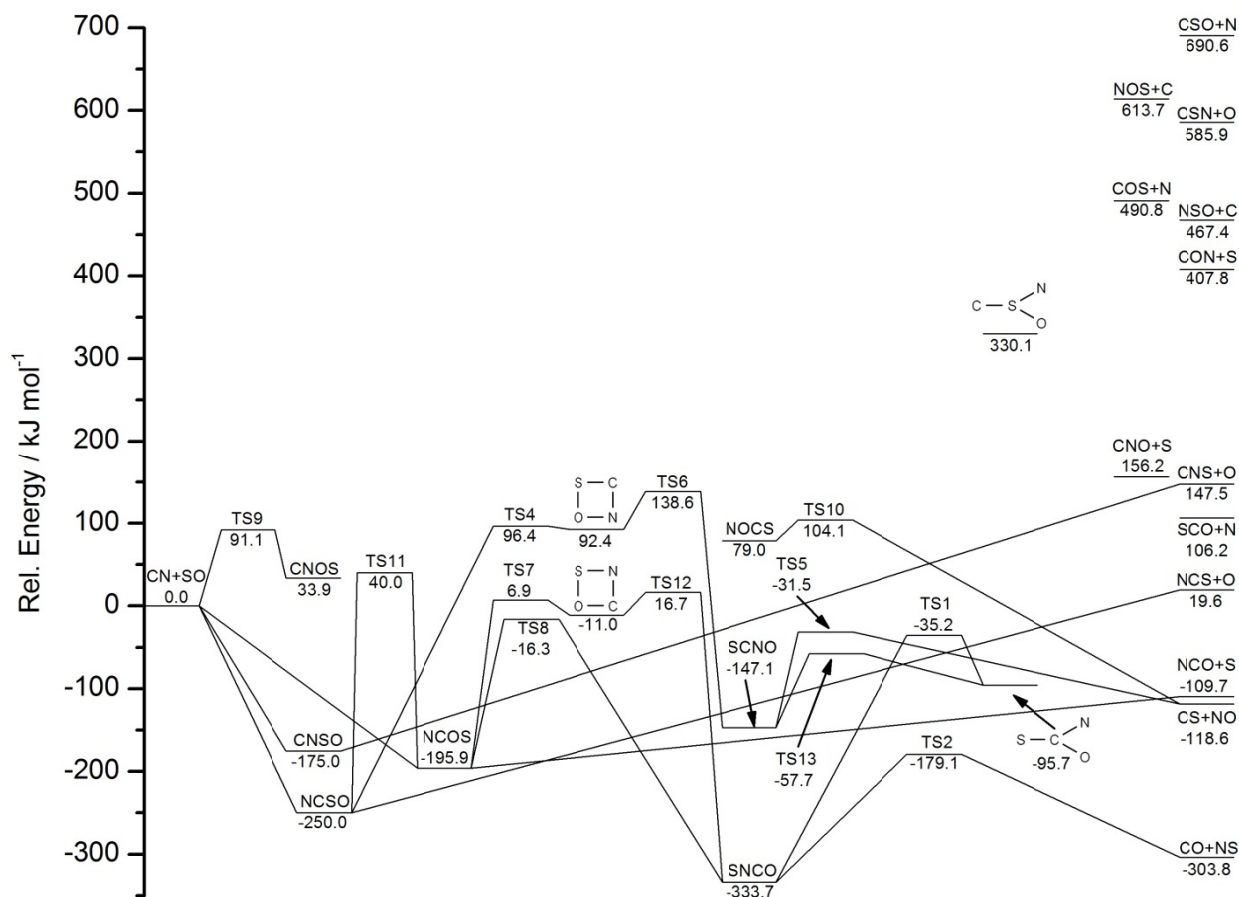
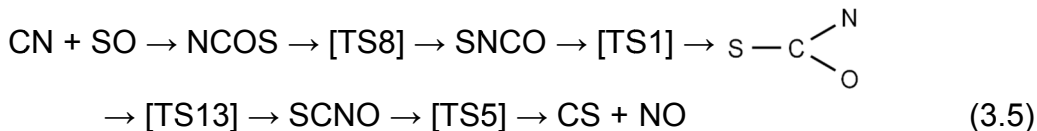


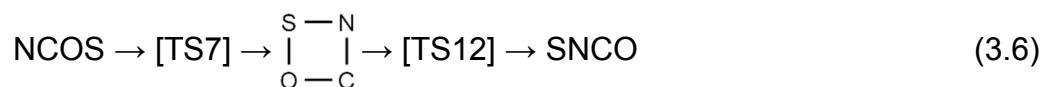
Figure 3.1. $^2\text{CN} + ^3\text{SO}$ doublet potential energy surface (QCISD/6-311G(d)).

The exothermic products are $\text{CO} + \text{NS}$ ($-303.8 \text{ kJ mol}^{-1}$), $\text{CS} + \text{NO}$ ($-118.6 \text{ kJ mol}^{-1}$) and $\text{NCO} + \text{S}$ ($-109.7 \text{ kJ mol}^{-1}$). All three product groups can be produced via reaction pathways which involve no barriers greater than the energy of the reactants.



See Figures 3.2 through 3.4 for images of the structural geometries for the reaction pathways shown in equation 3.3, 3.4 and 3.5, respectively. The reaction shown in

equation 3.4 may be one explanation for the experimental observation of NS molecules in flames by Jeffries and Crosley.⁷ The reaction shown in equation 3.5 is notable as a pathway to direct production of nitrogen oxide. As an alternative to the transition from NCOS to SNCO shown in equation 3.4 and 3.5, it may be possible for the reaction to proceed as



because the energy barriers, while positive, are only modest. Similarly, it may be possible for the barrierless process forming NCS + O from NCSO to occur.

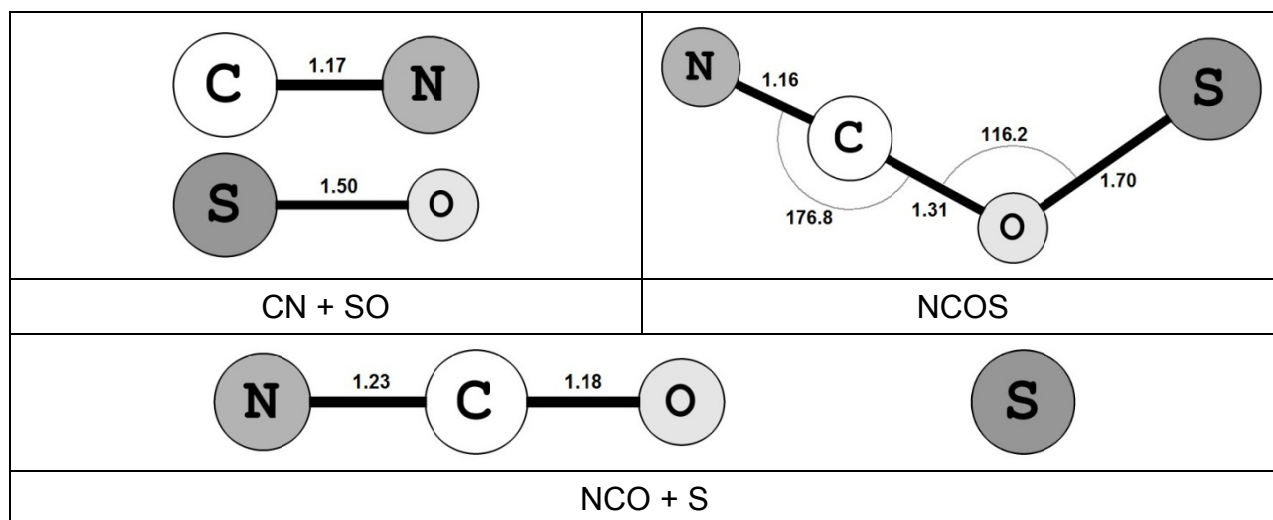


Figure 3.2. Minima and transition states for the reaction path producing NCO + S products. Distances in 10^{-10} m, angles in degrees.

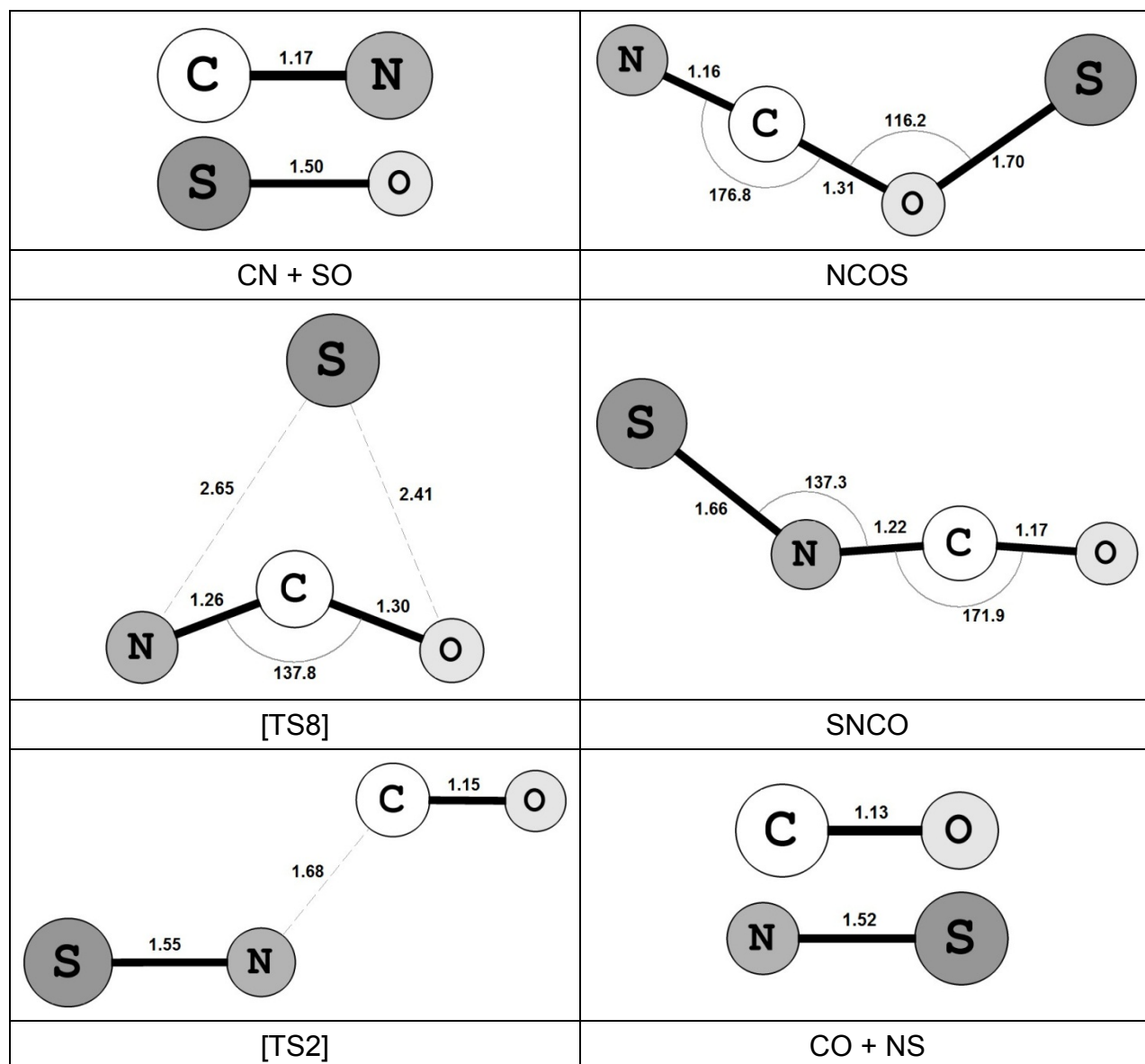


Figure 3.3. Minima and transition states for the reaction path producing CO + NS products. Distances in 10^{-10} m, angles in degrees.

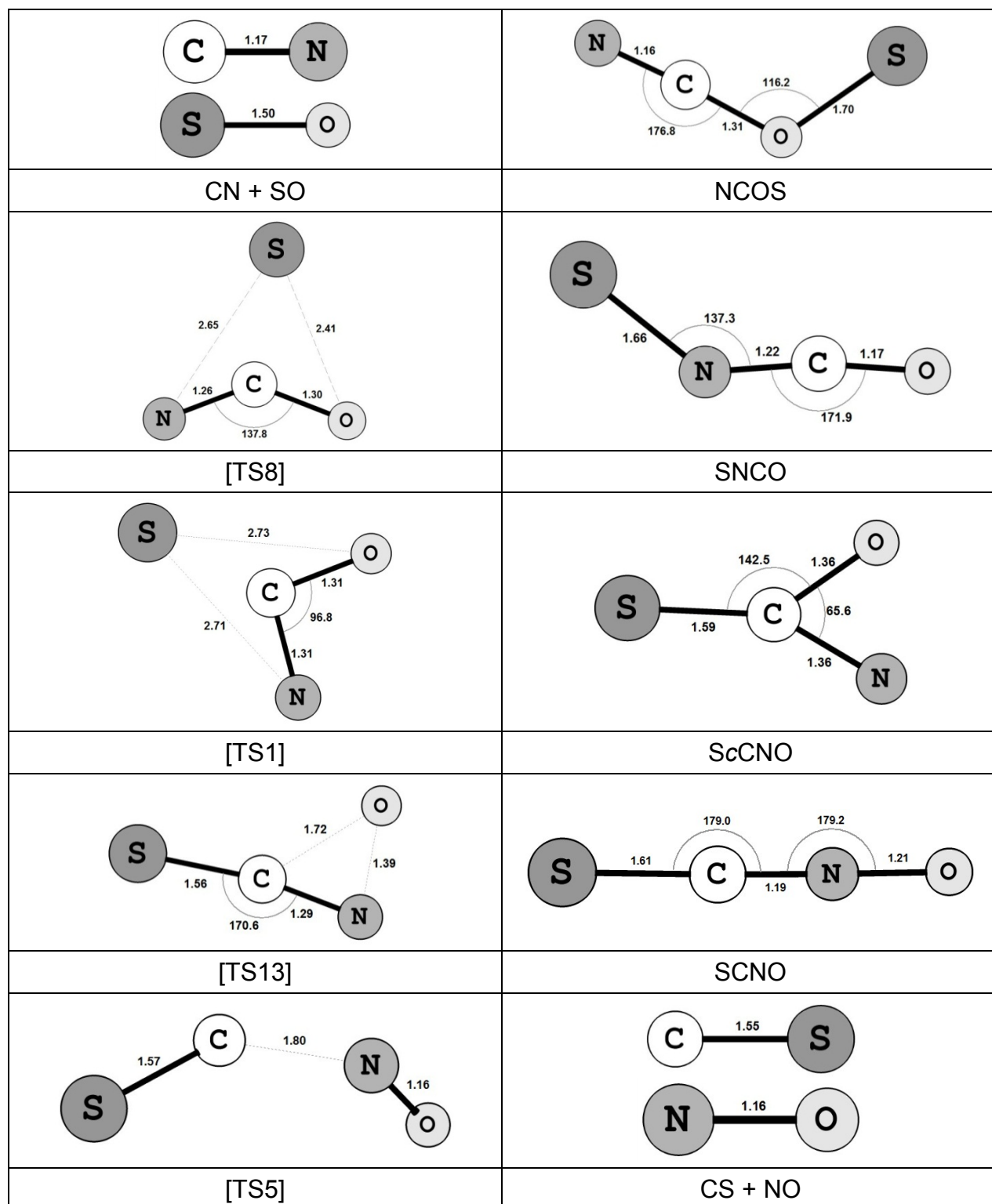
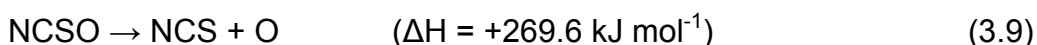
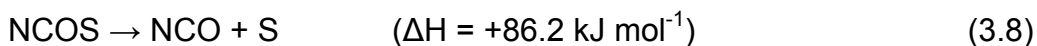
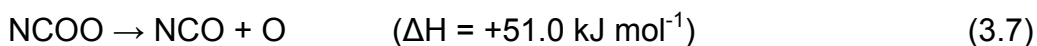
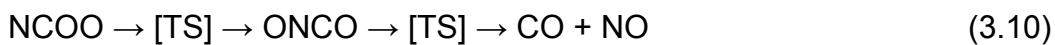


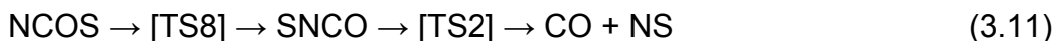
Figure 3.4. Minima and transition states for the reaction path producing CS + NO products. Distances in 10^{-10} m, angles in degrees.

Some pathways in the results for CN + SO are notably analogous to the PES (CCSD(T)) of the reaction between CN and O₂ as calculated by Qu et al.⁸ These similarities are not unexpected due to sulfur and oxygen being part of the same chemical group. However, despite the qualitative similarities, the relative energy levels are noticeably different between the two PES and in a way that is not explained simply by the difference in the potential energies of the reactant species. For example, in the CN + O₂ reaction, the intermediate NCOO produces NCO + O through a barrierless process, just as NCOS produces NCO + S and NCSO produces NCS + O through barrierless processes. Taking each species with respect to its own PES, NCOS (-195.9 kJ mol⁻¹) and NCSO (-250.0 kJ mol⁻¹) are both more stable adducts than NCOO (-133.9 kJ mol⁻¹). The NCSO → NCS + O process involves both the most stable adduct of the three as well as the least stable products, which ultimately gives that process a much larger ΔH, despite its similarity at first glance.



As another example, NCOO produces ONCO through a 1,3-shift, just as NCOS produces SNCO through a 1,3-shift. Interestingly, the barrier for this transition remains below the energy of the reactants in the CN + SO reaction, while the barrier is significantly endothermic in the CN + O₂ reaction. Subsequently, the NC bond in ONCO can break, leaving the NO + CO products while, in the CN + SO reaction, the NC bond in SNCO can break, leaving the NS + CO products.

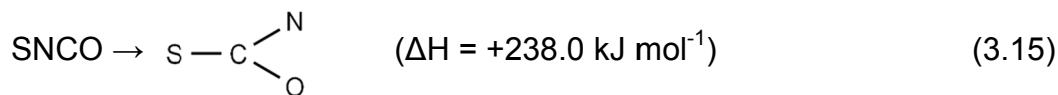
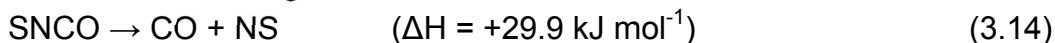
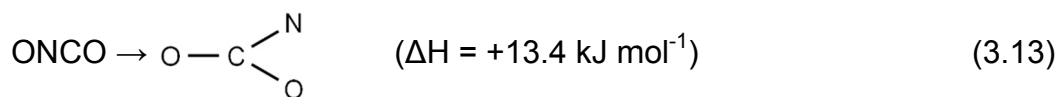
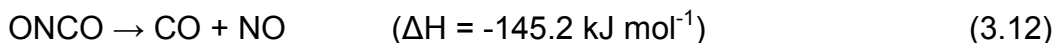




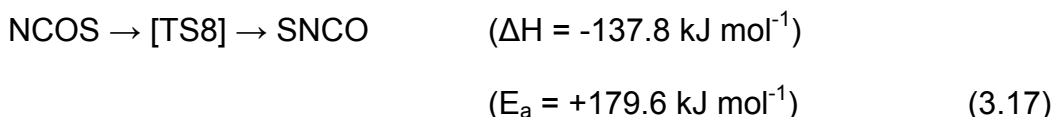
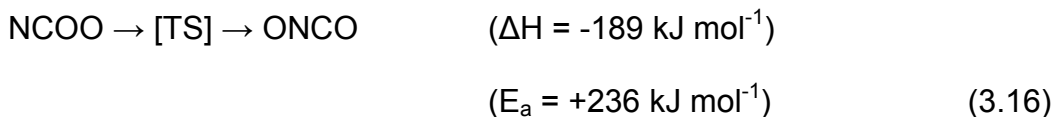
In both reactions, these product groups (NO + CO and NS + CO) are the most thermodynamically stable products on their respective PES. The latter transition in equation 3.10 is exothermic while the same is not true in equation 3.11. However, because of the barrier height in the CN + O₂ PES, the reaction involving sulfur may produce CO more rapidly.

Alternatively, the intermediate ONCO can instead transition to OcCNO (i.e. oxygen bonded to a carbon which is bonded to a nitrogen and a second oxygen) which then dissociates to CO₂ + N. The intermediate SNCO can similarly transition to ScCNO (sulfur bonded to a carbon which is bonded to a nitrogen and an oxygen), although the subsequent expected analogous process to the formation of CO₂ + N (i.e. the formation of OCS + N) has not been discovered. It is worth noting, however, that formation of OCS + N will necessarily have a barrier above the energy of the reactants. While there is a positive ΔH for formation of CO₂ + N in this way, the process remains exothermic relative to the energy of the reactants on the CN + O₂ PES.

Another similarity between the two PES is that the processes for formation of OcCNO and ScCNO are less thermodynamically and kinetically favorable than the dissociation pathways from the same reactants:



As with formation of OCS + N mentioned above, by comparison with the CN + O₂ potential energy surface there are expected to be additional transition states (and therefore reaction pathways) on the CN + SO potential energy surface which are currently unresolved. For example, looking to the CN + O₂ PES, the 1,3-shift of oxygen is seen between NCOO and ONCO. While there is a 1,3-shift of sulfur between NCOS and SNCO in the CN + SO PES, the analogous 1,3-shift of oxygen between NCOS and SCNO remains to be found. This transition is significant because it is possible it could provide a pathway to the formation of NO with only a modest energy barrier. Comparing the two processes which have been quantified, those of NCOO and NCOS, it is interesting to note that the trend in activation energy does not follow what might be expected given the linear relationship described by the Evans-Polanyi principle, which would expect a lower barrier height for the more exothermic process.⁹



Lastly, in the CN + O₂ PES the products CNO + O are produced by barrierless dissociation of oxygen from CNOO. In the CN + SO PES, CNSO produces CNS + O via barrierless dissociation, but the analogous CNOS dissociation to CNO + S has not yet been demonstrated.

Although the CN + SO PES discussed so far has been wholly concerning doublet intermediates, quartet intermediates are also possible intermediates in the reaction of a doublet and triplet. Quartet intermediate minima were optimized at the B3LYP/6-311G(d) level, as shown in Figure 3.5 below.

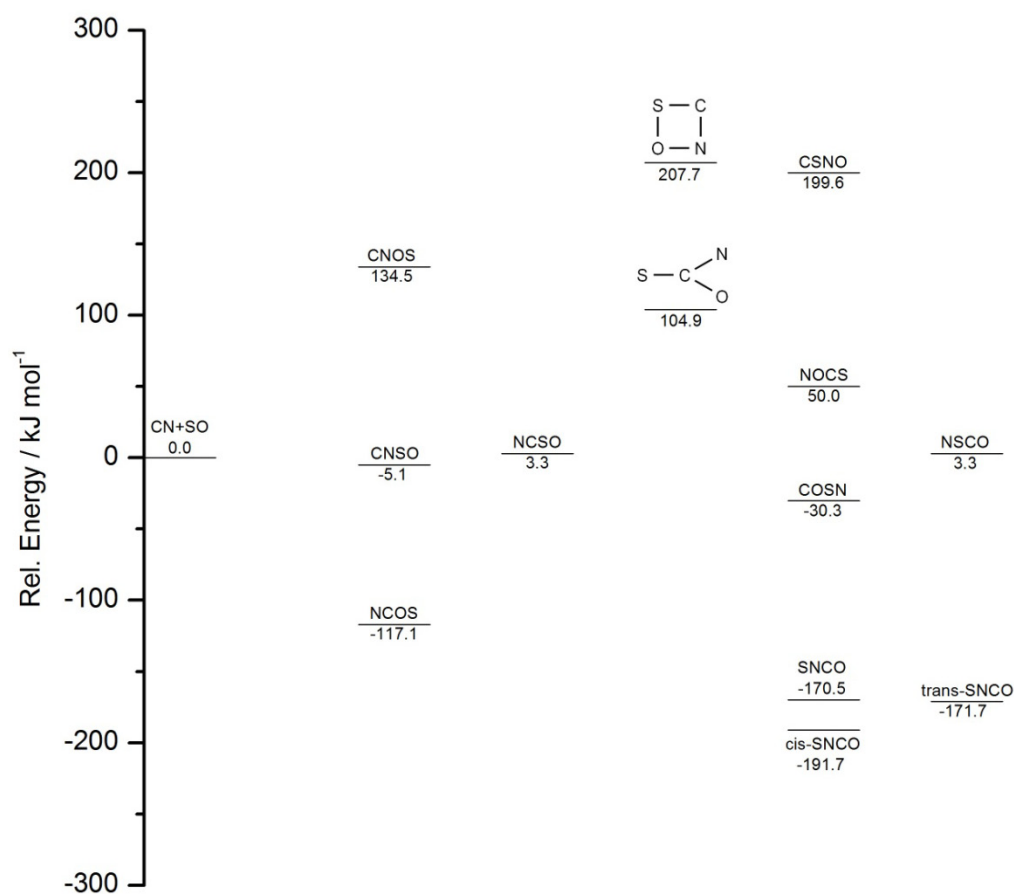


Figure 3.5. $^2\text{CN} + ^3\text{SO}$ quartet minima energy levels (B3LYP/6-311G(d)).

3.5 References

- (1) Jensen, F. *Introduction to Computational Chemistry*; John Wiley & Sons: Chichester, 1999.
- (2) Becke, A. D. *J. Chem. Phys.* **1992**, *98*, 1372.
- (3) Lee, C.; Yang, W.; Parr, R. G. *Phys. Rev. A* **1989**, *37*, 78.

- (4) Pople, J. A.; Head-Gordon, M.; Raghavachari, K. *J. Chem. Phys.* **1987**, *87*, 5968.
- (5) Krishnan, R.; Binkley, J. S.; Seeger, R.; Pople, J. A. *J. Chem. Phys.* **1980**, *72*, 650.
- (6) Frisch, M. J.; Trucks, G. W.; Schlegel, H. B.; Scuseria, G. E.; Robb, M. A.; Cheeseman, J. R.; Montgomery, J. A. J.; Vreven, T.; Kudin, K. N.; Burant, J. C.; Millam, J. M.; Iyengar, S. S.; Tomasi, J.; Barone, V.; Mennucci, B.; Cossi, M.; Scalmani, G.; Rega, N.; Petersson, G. A.; Nakatsuji, H.; Hada, M.; Ehara, M.; Toyota, K.; Fukuda, R.; Hasegawa, J.; Ishida, M.; Nakajima, T.; Honda, Y.; Kitao, O.; Nakai, H.; Klene, M.; Li, X.; Knox, J. E.; Hratchian, H. P.; Cross, J. B.; Bakken, V.; Adamo, C.; Jaramillo, J.; Gomperts, R.; Stratmann, R. E.; Yazyev, O.; Austin, A. J.; Cammi, R.; Pomelli, C.; Ochterski, J. W.; Ayala, P. Y.; Morokuma, K.; Voth, G. A.; Salvado, P.; Dannenburg, J. J.; Zakrzewski, V. G.; Dapprich, S.; Daniels, A. D.; Strain, M. C.; Farkas, O.; Malick, D. K.; Rabuck, A. D.; Raghavachari, K.; Foresman, J. B.; Ortiz, J. V.; Cui, Q.; Baboul, A. G.; Clifford, S.; Cioslowski, J.; Stefanov, B. B.; Liu, G.; Liashenko, A.; Piskorz, P.; Komaromi, I.; Martin, R. L.; Fox, D. J.; Keith, T.; A, A.-L. M.; Peng, C. Y.; Nanayakkara, A.; Challacombe, M.; Gill, P. M. W.; Johnson, B.; Chen, W.; Wong, M. W.; Gonzalez, C.; Pople, J. A. Gaussian 03, revision C.02; Gaussian, Inc. Wallingford, CT, 2004.
- (7) Jeffries, J. B.; Crosley, D. R. *Combust. Flame* **1986**, *64*, 55.
- (8) Qu, Z.; Zhu, H.; Li, Z.; Zhang, X.; Zhang, Q. *Chem. Phys. Lett.* **2002**, *353*, 304.
- (9) Evans, M. G.; Polanyi, M. *Trans. Faraday Soc.* **1936**, *32*, 1333.

CHAPTER 4

CONCLUSIONS

4.1 Experiment Conclusions

The kinetics of the reaction of atomic sulfur with acetylene was investigated over the temperature range 295 to 1015 K via laser flash photolysis and the resonance fluorescence detection method. The second order rate constant was found to be pressure-dependent at all experimental temperatures, suggesting formation of one or more adduct species able to be stabilized by collision. Using statistical mechanics to perform a rough analysis of calculated thermodynamic data for the reaction shows stable adduct species at all experimental temperatures, supporting this conclusion.

The Arrhenius equation obtained from the temperature dependence plot of the high-pressure limit rate constant is

$$k = ((2.14 \pm 0.19) \times 10^{-11} \text{ cm}^3 \text{ molecule}^{-1} \text{ s}^{-1}) e^{-((11.34 \pm 0.03) \text{ kJ mol}^{-1}) / RT}$$

which indicates a positive activation energy. Theoretical modeling of the intersystem crossing between ground-state triplet sulfur and excited-state singlet sulfur shows an energy barrier which is notably similar to the magnitude of the activation energy shown by the experiment. Concerning the intersystem crossing, the large values for the high-pressure limit rate constants, only an order of magnitude less than the idealized hard-sphere collision model, indicate an unusually fast rate for a spin-forbidden reaction.

The results of this experiment and analysis suggest stable adduct formation, especially in light of the theoretical potential energy surface, and therefore do not provide a path to production of HCS. It may be that the mechanism proposed for acetylene to produce CS₂ during the Claus process cannot proceed at the temperatures

used for the Claus process (which are within the range of the experimental temperatures for this investigation). In addition to expanding academic knowledge of sulfur chemistry, the quantitative results of this experiment may be applicable to diamond film deposition and soot formation, especially with regard to sulfur's influence on the kinetics and thermodynamics of vinylidene.

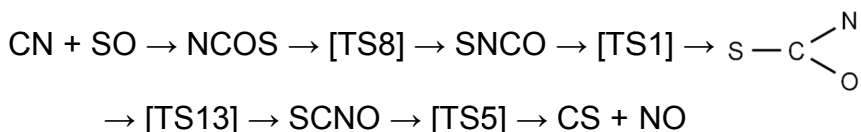
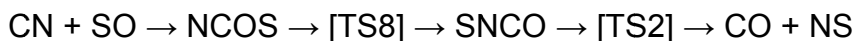
4.2 Theory Conclusions

The CN and SO radicals are likely to be present in combustion conditions due to the presence of sulfur, nitrogen and oxygen in fossil fuels. The CN radical is stable due to its strong triple-bond, and the SO radical is likely given the availability of oxygen. The products of this reaction include species which could have substantial impacts on combustion chemistry and the pollutant products of combustion.

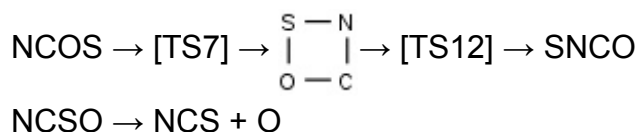
The majority of the potential energy surface (PES) for the reaction CN + SO was modeled by theory. The geometries and vibrational frequencies for the stationary points (local minima and maxima) were optimized initially using the B3LYP/6-311G(d) level of theory. These results were used as starting points for further optimization at the QCISD/6-311G(d) level of theory, ultimately resulting in the current PES. This surface was shown to be notably analogous to that of the reaction CN + O₂, albeit with significant differences in the relative energies of the stationary points.

There are three product groups, NCO + S, CO + NS and CS + NO which are shown to be produced via reaction paths which contain no barriers greater in energy than reactants:





The second may explain the observation of NS in flames, and may produce CO more rapidly than the analogous process in the reaction of $\text{CN} + \text{O}_2$. The latter is notable as a direct path to production of nitrogen oxide. There are two reaction path segments with modest energy barriers that may be viable at combustion temperatures:



Additional transition states on the PES are expected, but have not yet been resolved. There may be a reaction pathway with a modest energy barrier to formation of the SCNO intermediate (and therefore direct production of NO). Ultimately, the QCISD/6-311G(d) geometries will be used to calculate more accurate energy values via the CCSD(T) level of theory extrapolated to the infinite basis set limit. These energy values will produce the final potential energy surface, which will be accurate enough for use as the basis of a theoretical kinetics analysis via Rice–Ramsperger–Kassel–Marcus (RRKM) theory.

APPENDIX A
FLOW CONTROLLER CALIBRATION

Flow controller
#1

	Flow 2 1 cc	Flow 6 3 cc	Flow 10 5 cc	Flow 14 7 cc	Flow 18 10 cc
	24.14	25.8	26	26.13	29.38
	23.94	25.16	25.66	26.24	29.56
	23.93	25.66	25.84	26.16	29.53
	23.88	25.22	25.8	26.1	29.56
	23.97	25.37	25.67	25.87	29.39
avg sec	23.97	25.44	25.79	26.10	29.48
avg min	0.399533	0.424033	0.4299	0.435	0.4914
massflow cc/min	2.50292	7.074915	11.63061	16.09195	20.35002
massflow corrected	2.436593	6.88743	11.3224	15.66552	19.81074

Flow Controller #2

	Flow 10 10 cc	Flow 30 20 cc	Flow 50 30 cc	Flow 70 50 cc	Flow 90 100 cc
	61.14	38.6	35.28	41.73	64.88
	62.87	38.97	35.29	41.7	65.33
	62.24	38.85	35.12	41.61	64.78
	63.54	39.01	35.03	41.6	64.93
	58.05	38.79	34.79	41.75	65.03
avg sec	61.57	38.84	35.10	41.68	64.99
avg min	1.026133	0.6474	0.585033	0.694633	1.083167
massflow cc/min	9.745322	30.8928	51.27913	71.98042	92.3219
massflow corrected	9.617659	30.48811	50.60737	71.03748	91.11248

Flow controller
#3

	Flow 200 100 cc	Flow 600 300 cc	Flow 1000 500 cc	Flow 1400 700 cc	Flow 1800 1000 cc
	29.65	30.78	31.01	30.56	34.39
	30.31	30.54	30.65	30.83	34.38
	29.98	30.47	30.3	30.67	34.86
	30.03	30.66	31.09	30.7	34.24
	30.54	30.55	31.11	30.6	34.26
avg sec	30.10	30.60	30.83	30.67	34.43
avg min	0.5017	0.51	0.513867	0.5112	0.573767
massflow cc/min	199.3223	588.2353	973.015	1369.327	1742.869
massflow corrected	194.0403	572.6471	947.2302	1333.04	1696.683

Flow controller #4

	Flow 5 5 cc	Flow 15 10 cc	Flow 25 20 cc	Flow 35 20 cc	Flow 45 50 cc
	44.07	29.45	34.76	24.85	48.04
	43.71	29.77	34.44	25.28	51.18
	44.85	28.98	34.53	25.02	48.54
	44.86	29.99	35.95	24.38	48.14
	45.3	29.26	35.23	24.47	48.25
avg sec	44.56	29.49	34.98	24.80	48.83
avg min	0.742633	0.4915	0.583033	0.413333	0.813833
massflow cc/min	6.732798	20.34588	34.30336	48.3871	61.43764
massflow corrected	6.554379	19.80671	33.39432	47.10484	59.80954

APPENDIX B
S + C₂H₂ KINETICS DATA

T / K	τ / s	F / mJ	P / Torr	$[\text{CS}_2] / 10^{13} \text{ cm}^{-3}$ molecule	$[\text{S}]_0 / 10^{11} \text{ cm}^{-3}$ molecule	$[\text{C}_2\text{H}_2]_{\text{max}} / 10^{14} \text{ cm}^{-3}$ molecule	$[\text{H}]_{\text{max}} / 10^9 \text{ cm}^{-3}$ molecule	$k_1 / 10^{-13} \text{ cm}^3 \text{ molecule}^{-1} \text{ s}^{-1}$	$\sigma_k / 10^{-13} \text{ cm}^3 \text{ molecule}^{-1} \text{ s}^{-1}$	$[\text{Ar}] / 10^{17} \text{ cm}^{-3}$ molecule	
298	2.06	0.056	50.6	25.40	50.32	41.70	42.11	1.46	\pm	0.03	16.40
298	0.59	0.050	10.1	55.10	93.68	16.10	14.52	1.09	\pm	0.01	3.25
298	1.22	0.050	20.2	26.00	45.96	16.70	15.06	1.43	\pm	0.04	6.53
298	3.08	0.050	50.8	38.10	66.26	28.20	25.43	1.78	\pm	0.08	16.40
297	3.10	0.028	51.0	38.30	37.29	43.50	21.96	1.68	\pm	0.06	16.60
297	3.14	0.117	51.6	38.70	157.36	43.90	92.62	1.84	\pm	0.07	16.70
297	0.61	0.024	10.1	13.00	11.22	39.90	17.27	0.98	\pm	0.04	3.26
297	0.62	0.024	10.2	22.70	19.34	40.20	17.40	1.19	\pm	0.08	3.30
297	0.61	0.024	10.2	41.30	34.33	39.50	17.10	0.96	\pm	0.03	3.29
297	3.20	0.020	101.4	4.90	3.56	43.10	15.54	1.90	\pm	0.11	32.90
298	4.14	0.041	101.7	25.50	36.98	41.70	30.83	1.81	\pm	0.06	32.90
296	2.15	0.036	101.6	22.80	29.14	21.60	14.02	1.85	\pm	0.08	33.10
296	2.06	0.036	50.3	21.90	28.02	20.70	13.44	1.79	\pm	0.04	16.40
296	2.08	0.037	50.8	11.10	14.81	20.90	13.95	1.80	\pm	0.09	16.60
296	2.10	0.037	51.2	6.50	8.73	21.10	14.08	1.74	\pm	0.10	16.70
295	1.24	0.051	20.5	25.00	45.13	18.80	17.29	1.34	\pm	0.01	6.68
295	3.09	0.051	50.7	39.20	69.43	31.40	28.88	1.74	\pm	0.09	16.60
295	3.37	0.053	82.0	30.10	56.08	20.80	19.88	1.84	\pm	0.10	26.80
295	4.36	0.053	205.6	32.40	60.18	22.50	21.51	2.26	\pm	0.15	66.90
295	3.86	0.053	152.6	34.50	63.91	31.60	30.20	2.38	\pm	0.17	49.90
295	1.95	0.055	151.2	32.10	61.90	39.30	38.98	1.54	\pm	0.07	49.50
295	2.75	0.055	151.0	32.90	63.38	55.70	55.24	1.52	\pm	0.06	49.40
295	3.84	0.055	152.0	34.40	66.13	39.10	38.78	1.63	\pm	0.07	49.70
295	5.20	0.054	403.4	32.80	62.04	46.40	45.18	2.08	\pm	0.16	132.00
296	4.90	0.054	306.0	32.30	61.14	41.90	40.80	2.10	\pm	0.16	99.80

367	0.53	0.030	10.7	4.71	5.14	21.30	11.52	1.96	±	0.02	2.81
367	0.53	0.030	10.9	8.75	9.50	21.50	11.63	2.13	±	0.05	2.86
367	0.52	0.030	10.9	16.50	17.72	21.30	11.52	2.16	±	0.04	2.86
366	0.55	0.023	11.1	8.15	6.79	22.00	9.13	2.06	±	0.03	2.92
366	0.55	0.041	11.2	8.22	12.20	22.20	16.42	2.22	±	0.04	2.95
366	0.55	0.079	11.3	8.28	23.68	22.40	31.92	2.23	±	0.02	2.97
367	1.02	0.034	20.9	7.03	8.67	21.00	12.88	2.95	±	0.04	5.48
367	1.70	0.034	50.7	6.86	8.46	23.50	14.41	3.74	±	0.12	13.30
367	1.66	0.034	81.8	6.70	8.27	23.00	14.10	3.88	±	0.09	21.50
365	1.73	0.034	101.0	6.99	8.62	23.90	14.66	4.23	±	0.09	26.70
364	4.22	0.031	404.3	6.69	7.52	20.60	11.52	5.13	±	0.60	107.00
366	3.95	0.032	305.4	6.65	7.72	19.20	11.08	4.29	±	0.41	80.60
366	4.07	0.032	200.0	6.86	7.96	19.80	11.43	4.73	±	0.16	52.70
459	0.44	0.032	11.3	3.95	4.60	9.10	5.25	3.39	±	0.04	2.36
459	0.44	0.032	11.3	7.25	8.41	9.03	5.21	3.46	±	0.06	2.37
459	0.44	0.032	11.4	1.38	1.61	9.00	5.19	3.67	±	0.06	2.38
459	0.44	0.020	11.4	5.64	4.10	9.14	3.30	3.34	±	0.03	2.38
459	0.44	0.042	11.5	5.69	8.68	9.22	6.98	3.33	±	0.06	2.41
459	0.45	0.085	11.4	5.67	17.51	9.22	14.14	3.52	±	0.04	2.40
461	0.80	0.036	20.9	6.15	8.04	9.57	6.21	4.68	±	0.09	4.38
461	1.34	0.036	50.4	5.60	7.33	10.60	6.88	6.48	±	0.10	10.60
459	2.82	0.035	304.8	5.87	7.46	12.50	7.89	9.19	±	0.52	64.10
459	2.38	0.035	203.0	5.79	7.36	10.60	6.69	8.42	±	0.30	42.70
459	1.66	0.035	102.6	5.78	7.35	9.92	6.26	7.52	±	0.13	21.60
721	0.65	0.042	50.9	2.88	4.41	8.04	6.09	9.48	±	0.11	6.82

721	0.65	0.042	51.2	5.51	8.41	8.04	6.09	9.74	±	0.12	6.86
720	0.26	0.040	10.7	5.78	8.40	7.79	5.62	4.54	±	0.09	1.43
719	0.26	0.042	20.4	5.82	8.88	7.90	5.98	6.39	±	0.05	2.73
719	0.26	0.020	20.5	5.85	4.25	7.94	2.86	6.22	±	0.07	2.75
719	0.26	0.091	20.5	5.86	19.37	7.94	13.03	6.49	±	0.05	2.75
720	0.65	0.051	51.0	5.74	10.64	8.78	8.08	10.18	±	0.11	6.83
720	0.64	0.051	51.1	11.10	20.42	8.68	7.98	10.40	±	0.04	6.85
720	0.64	0.051	50.4	2.99	5.56	8.74	8.04	10.25	±	0.04	6.76
719	1.03	0.042	100.8	5.64	8.61	8.45	6.40	14.27	±	0.19	13.50
719	2.09	0.042	202	5.68	8.67	8.58	6.50	19.23	±	0.23	27.10
720	1.06	0.042	202	5.68	8.67	8.67	6.57	19.19	±	0.24	27.10
719	2.12	0.040	403	4.02	5.86	5.31	3.83	21.74	±	0.36	54.10
720	1.98	0.041	302	4.11	6.14	3.05	2.26	19.87	±	0.16	40.50
719	2.13	0.041	402	4.41	6.58	3.27	2.42	21.42	±	0.27	54.00
1012	0.61	0.049	51.1	6.61	11.75	12.90	11.40	6.22	±	0.08	4.87
1012	0.31	0.049	50.4	6.35	11.29	13.00	11.49	7.18	±	0.10	4.80
1013	0.38	0.049	102	6.60	11.74	12.10	10.69	12.27	±	0.12	9.72
1013	0.76	0.05	203	6.60	11.98	4.76	4.29	15.70	±	0.30	19.30
1012	1.49	0.053	203	6.61	12.71	4.62	4.42	11.60	±	0.53	19.40
1014	1.5	0.05	204	6.64	12.05	4.64	4.18	9.88	±	0.37	19.40
1014	0.74	0.05	101	6.55	11.88	4.53	4.09	9.59	±	0.07	9.62
1013	0.31	0.052	50.5	6.67	12.59	7.88	7.39	7.04	±	0.08	4.81
1012	0.46	0.05	51	6.68	12.12	9.40	8.48	6.74	±	0.21	4.86
1012	0.6	0.05	50.8	6.67	12.10	12.30	11.09	6.29	±	0.16	4.84
1014	0.72	0.057	50.8	6.68	13.82	11.70	12.03	6.27	±	0.16	4.83
1014	0.87	0.057	50.6	6.68	13.82	14.30	14.70	5.52	±	0.17	4.81
1013	0.46	0.05	50.8	4.31	7.84	9.38	8.46	7.13	±	0.07	4.83

1013	0.46	0.05	50.8	6.26	11.36	9.34	8.42	7.08	±	0.11	4.84
1013	0.46	0.05	50.9	8.21	14.86	9.33	8.41	7.12	±	0.14	4.85
1013	0.87	0.05	50.4	6.65	12.07	14.20	12.81	5.75	±	0.09	4.79
1014	0.29	0.052	101.4	6.67	12.59	5.56	5.22	13.71	±	0.09	9.66
1015	0.38	0.052	100.8	6.57	12.40	7.15	6.71	12.44	±	0.11	9.59
1014	0.47	0.052	100.6	6.67	12.59	8.83	8.28	11.75	±	0.09	9.58
1015	0.62	0.052	100.4	6.52	12.30	7.86	7.37	10.89	±	0.24	9.55
1013	0.74	0.052	100.8	6.64	12.53	7.57	7.10	10.96	±	0.14	9.61
1012	0.58	0.05	202	6.62	12.01	5.44	4.91	19.66	±	0.31	19.30
1015	0.76	0.05	204	6.63	12.03	5.92	5.34	17.83	±	0.25	19.40
1015	0.93	0.05	200.8	6.60	11.98	5.82	5.25	16.64	±	0.22	19.10
1015	1.24	0.05	202	6.52	11.83	6.22	5.61	14.96	±	0.29	19.20
1013	1.5	0.05	203.8	6.65	12.07	7.50	6.76	14.14	±	0.20	19.40

APPENDIX C

S + C₂H₂ ADDUCT DATA USED FOR STATISTICAL
MECHANICS CALCULATIONS

	Symmetry	Rotational Constants (GHz)	Moments of Inertia (kg m ²)	Vibrational Frequencies (cm ⁻¹)			ΔH (kJ mol ⁻¹)
H ₂ CCS	C _{2v} ($\sigma = 2$)	289.069 5.687957 5.578196	2.903×10^{-47} 1.475×10^{-45} 1.504×10^{-45}	366.2 860.1 1813.4	425.5 935.2 3142.4	720.5 1379.1 3220.3	-303.8
HCCSH	C _s ($\sigma = 1$)	291.0654 5.568715 5.464174	2.883×10^{-47} 1.507×10^{-45} 1.536×10^{-45}	300.7 714.2 2152.4	364.3 727.2 2647.4	579.9 980.5 3471	-245.4
HC(S)CH	C _{2v} ($\sigma = 2$)	34.26846 10.94742 8.296893	2.449×10^{-46} 7.666×10^{-46} 1.011×10^{-45}	452.7 781.9 1747.2	598.7 907 3269.8	660.3 940.4 3326.4	-170.2
C(S)CH ₂	C _s ($\sigma = 1$)	29.78744 12.37138 9.272477	2.817×10^{-46} 6.783×10^{-46} 9.050×10^{-46}	592.7 955 1460.8	785.1 988.2 3089.7	892.2 1130.3 3170.1	-115.5
CCHSH	C ₁ ($\sigma = 1$)	35.96866 10.01694 8.269895	2.333×10^{-46} 8.378×10^{-46} 1.015×10^{-45}	358 684.3 1653.6	555.6 960.9 2578.2	657.8 987.9 3287.9	-84.2
3-C ₂ H ₂ S	C _s ($\sigma = 1$)	53.14081 7.03362 6.21148	1.579×10^{-46} 1.193×10^{-45} 1.351×10^{-45}	339.5 860.8 1384.5	713.6 895.3 3131.6	769.2 1257.4 3212.2	-60.7

C₂H₂ C _{∞ v} ($\sigma = 2$) B = 35.28072 GHz I = 2.379×10^{-46} kg m²
Frequencies (cm⁻¹) = 3373.7 1973.8 3281.9 611.6 611.6 729.3 729.3

Sulfur ³p₂ (g=5)
³p₁ (g=3) 4.738 kJ mol⁻¹
³p₀ (g=1) 6.862 kJ mol⁻¹

* C₂H₂ and sulfur data from JANAF thermochemical tables.

* Singlet adduct rotational constants were obtained via single-point HF/STO-3G calculations using geometries from Leonori et al. Vibrational frequencies from Leonori et al.

* Triplet adduct rotational constants and vibrational frequencies were obtained via single-point HF/STO-3G calculations using B3LYP optimized geometries. (bond lengths from Woon).


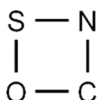
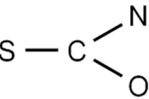
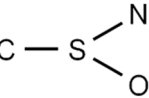
APPENDIX D

CN + SO GEOMETRIES, ENERGIES AND FREQUENCIES

Table D.1. QCISD / 6-311G(d) doublet potential energy surface

	Cartesian Coordinates (Å)				Energy (Hartrees)	ZPE (Hartrees)	E _{tot} (Hartrees)	Vibrational Frequencies (cm ⁻¹)	
CN	C	0.000000	0.000000	-0.632595	-92.50567	0.00491	-92.50076	2155	
	N	0.000000	0.000000	0.542225					
3-SO	S	0.000000	0.000000	0.500906	-472.68302	0.00259	-472.68043	1136	
	O	0.000000	0.000000	-1.001811					
C					-37.76560		-37.76560		
S					-397.59830		-397.59830		
O					-74.93279		-74.93279		
2-N					-54.37850		-54.37850		
4-N					-54.49059		-54.49059		
CO	C	0.000000	0.000000	-0.647396	-113.08183	0.00499	-113.07684	2190	
	O	0.000000	0.000000	0.485547					
NS	N	0.000000	0.000000	-1.053918	-452.22273	0.00267	-452.22006	1172	
	S	0.000000	0.000000	0.461089					
CS	C	0.000000	0.000000	-1.124103	-435.60469	0.00293	-435.60176	1288	
	S	0.000000	0.000000	0.421539					
NO	N	0.000000	0.000000	-0.617938	-129.62881	0.00422	-129.62459	1853	
	O	0.000000	0.000000	0.540696					
CNO	C	0.000000	0.000000	-1.331352	-167.53213	0.00871	-167.52342	317	398
	N	0.000000	0.000000	-0.121171				1179	1930
	O	0.000000	0.000000	1.104538					
CNS	C	0.000000	0.000000	-1.847683	-490.19971	0.00751	-490.19221	244	287
	N	0.000000	0.000000	-0.654521				734	2030
	S	0.000000	0.000000	0.979234					
CON	C	1.023537	0.765584	0.000000	-167.43531	0.00774	-167.42757	192	691
	O	0.000000	0.220154	0.000000				2514	
	N	-0.877318	-0.907819	0.000000					
COS	C	0.687608	-0.923846	0.000000	-510.62130	0.00554	-510.61576	319	492
	O	-0.515706	-1.034068	0.000000				1621	
	S	0.000000	0.863476	0.000000					

CSN	C	1.609700	0.199823	0.000000	-490.02993	0.00468	-490.02524	175 847 1034
	N	-1.379743	-0.552150	0.000000				
	S	0.000000	0.166632	0.000000				
CSO	C	1.610502	0.218190	0.000000	-510.54445	0.00478	-510.53967	202 752 1144
	S	0.000000	0.251276	0.000000				
	O	-1.207877	-0.666195	0.000000				
NCS	C	0.000000	0.000000	-0.626565	-490.24888	0.00794	-490.24093	340 397 728 2020
	N	0.000000	0.000000	-1.807011				
	S	0.000000	0.000000	1.025529				
NCO	C	0.000000	0.000000	-0.039703	-167.63455	0.00989	-167.62466	505 578 1282 1976
	N	0.000000	0.000000	-1.269958				
	O	0.000000	0.000000	1.140990				
NOS	N	1.240885	1.056220	0.000000	-527.18628	0.00443	-527.18185	329 615 1000
	O	0.000000	0.766371	0.000000				
	S	-0.542887	-0.845282	0.000000				
NSO	N	1.417293	-0.213417	0.000000	-527.24363	0.00606	-527.23757	361 1076 1223
	S	0.000000	0.331960	0.000000				
	O	-1.240132	-0.477179	0.000000				
SCO	S	0.000000	0.000000	1.042518	-510.77142	0.00919	-510.76224	518 518 874 2122
	C	0.000000	0.000000	-0.530146				
	O	0.000000	0.000000	-1.687427				
CNSO	C	-1.182994	-1.882395	0.000000	-565.25809	0.01025	-565.24785	130 198 416 611 1072 2069
	N	-0.677829	-0.806286	0.000000				
	S	0.000000	0.757601	0.000000				
	O	1.480345	0.602094	0.000000				
CNOS	C	2.258803	-0.410831	-0.000803	-565.17894	0.01065	-565.16829	154 251 449 724 940 2155
	N	1.167696	0.049148	0.001206				
	O	0.016016	0.729341	-0.000383				
	S	-1.365926	-0.232111	-0.000035				
NCSO	C	-0.657076	-0.816566	0.000000	-565.28721	0.01079	-565.27642	180 296 462 631 978 2191
	N	-1.159646	-1.869956	0.000000				
	S	0.000000	0.803708	0.000000				
	O	1.507497	0.641221	0.000000				
NCOS	C	1.145768	0.105007	0.000000	-565.26801	0.01220	-565.25581	204 468 537 722 1084 2339
	N	2.194116	-0.398120	0.000000				
	O	0.000000	0.736983	0.000000				
	S	-1.389589	-0.233691	0.000000				

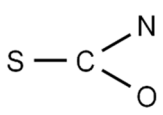
NOCS	C	0.000000	0.387708	0.000000	-565.16050	0.00940	-565.15111	141	240
	O	1.075240	-0.435723	0.000000				433	938
	N	2.287222	0.149325	0.000000				1089	1284
	S	-1.538279	0.007141	0.000000					
SCNO	C	0.000000	0.049711	0.000000	-565.24926	0.01203	-565.23724	219	258
	N	0.370587	-1.079099	0.000000				433	673
	S	-0.527901	1.571238	0.000000				1359	2336
	O	0.731538	-2.235548	0.000000					
SNCO	C	1.132684	0.031157	0.000000	-565.32126	0.01295	-565.30831	127	528
	S	-1.556710	-0.101497	0.000000				602	703
	N	0.000000	0.488231	0.000000				1418	2306
	O	2.263906	-0.247576	0.000000					
	S	0.000000	0.984100	0.000000	-565.15719	0.01117	-565.14602	407	567
	O	0.969893	-0.477750	0.000000				640	759
	C	-1.045577	-0.400197	0.000000				935	1596
	N	-0.212239	-1.360344	0.000000					
	S	0.000000	0.903325	0.000000	-565.19750	0.01210	-565.18540	498	567
	O	-1.062775	-0.509802	0.000000				601	898
	N	1.134712	-0.458866	0.000000				1162	1583
	C	0.093202	-1.193785	0.000000					
	C	0.000000	0.234987	0.000000	-565.22891	0.01125	-565.21766	412	446
	S	-0.391038	-1.310117	0.000000				602	847
	N	-0.328116	1.558756	0.000000				1026	1605
	O	1.069178	1.080081	0.000000					
	C	1.297663	-0.902080	0.000317	-565.06462	0.00914	-565.05548	265	266
	S	-0.135844	-0.080640	-0.000360				416	756
	O	-1.582399	-0.004869	0.000342				933	1375
	N	1.006674	0.963096	0.000160					
TS1	C	0.000000	0.368745	0.000000	-565.20342	0.00881	-565.19461	-378	354
	S	-0.089055	-1.296649	0.000000				466	639
	N	-0.949296	1.274336	0.000000				1100	1306
	O	1.008743	1.201695	0.000000					
TS2	C	1.117433	-0.764269	0.000000	-565.25834	0.00895	-565.24940	-866	135
	S	-1.550098	0.424145	0.000000				246	403
	N	0.000000	0.491210	0.000000				1118	2026
	O	2.262121	-0.704897	0.000000					

TS4	S	0.000000	0.979541	0.000000	-565.15418	0.00969	-565.14449	-601	386
	O	1.047369	-0.431211	0.000000				556	715
	C	-1.024915	-0.390404	0.000000				900	1696
	N	-0.318495	-1.411507	0.000000					
TS5	C	-0.233230	0.586895	-0.366139	-565.20214	0.00896	-565.19318	-602	93
	N	1.349334	0.284173	0.428089				236	473
	S	-1.546586	-0.165797	0.049641				1175	1957
	O	2.087428	-0.357229	-0.199254					
TS6	S	-1.071906	-0.303918	0.000000	-565.13827	0.00986	-565.12841	-534	379
	O	1.071824	-0.733383	0.000000				586	786
	C	0.000000	0.970298	0.000000				872	1705
	N	1.225129	0.701137	0.000000					
TS7	S	0.000000	0.994643	0.000000	-565.18930	0.01072	-565.17858	-576	482
	O	-1.059629	-0.456899	0.000000				570	770
	N	1.181790	-0.731747	0.000000				1188	1697
	C	0.034084	-1.189477	0.000000					
TS8	C	0.000000	0.596997	0.000000	-565.19731	0.00990	-565.18742	-268	348
	S	-0.206716	-1.173895	0.000000				572	683
	N	-1.004006	1.354049	0.000000				1046	1694
	O	1.291937	0.715249	0.000000					
TS9	C	-2.506892	-0.060597	0.000059	-565.15384	0.00766	-565.14618	-787	32
	N	-1.322581	-0.270879	0.000108				152	348
	O	0.119958	0.627031	0.000087				896	1933
	S	1.458734	-0.172282	-0.000113					
TS10	C	0.000000	0.566402	0.000000	-565.14881	0.00726	-565.14155	-1049	97
	O	1.064284	-0.623495	0.000000				274	432
	N	2.310058	-0.495392	0.000000				1079	1305
	S	-1.542792	0.316081	0.000000					
TS11	C	0.000000	0.795611	0.000000	-565.17575	0.00962	-565.16613	-1271	317
	N	-0.118142	1.967693	0.000000				396	641
	S	-0.486499	-0.955519	0.000000				755	2114
	O	1.076373	-0.407401	0.000000					
TS12	S	0.000000	0.998631	0.000000	-565.18530	0.01047	-565.17483	-941	392
	O	-1.079812	-0.767081	0.000000				497	811
	N	1.129933	-0.409123	0.000000				1197	1698
	C	0.121495	-1.162932	0.000000					

TS13	C	0.000000	0.268941	0.000000	-565.21292	0.00977	-565.20315	-483	348
	S	-1.245555	-0.672257	0.000000				425	788
	N	0.889689	1.207004	0.000000				997	1729
	O	1.712632	0.086679	0.000000					

Table D.2. B3LYP / 6-311G(d) quartet potential energy surface

	Cartesian Coordinates (Å)				Energy (Hartrees)	ZPE (Hartrees)	E _{tot} (Hartrees)	Vibrational Frequencies (cm ⁻¹)	
CNSO	C	-0.001488	-3.328520	0.000000	-566.13869	0.00795	-566.13074	25	58
	N	-0.001053	-2.164118	0.000000				66	75
	S	0.000000	0.958769	0.000000				1106	2158
	O	0.002038	2.472456	0.000000					
CNOS	C	2.381306	-0.613752	0.000007	-566.08705	0.00948	-566.07757	106	259
	N	1.408280	0.076018	-0.000011				347	402
	O	0.384864	0.801637	0.000005				1072	1976
	S	-1.701544	-0.203919	0.000000					
NCSO	C	-1.342223	-0.000112	0.000001	-566.13668	0.00913	-566.12755	108	212
	N	-2.505458	0.000118	0.000002				401	403
	S	0.540955	-0.000059	0.000000				731	2152
	O	2.117033	0.000099	-0.000002					
NCOS	C	1.162263	1.154138	0.000000	-566.18347	0.01008	-566.17339	34	73
	N	2.350792	1.400199	0.000000				510	588
	O	0.000000	0.914742	0.000000				1298	1921
	S	-1.464320	-1.502760	0.000000					
NOCS	C	0.000000	0.730508	0.000000	-566.11950	0.00974	-566.10976	200	393
	O	1.285350	0.396149	0.000000				608	870
	N	1.661414	-0.902655	0.000000				884	1321
	S	-1.369544	-0.077104	0.000000					
SNCO	C	1.176523	0.504356	0.000000	-566.20529	0.01157	-566.19372	103	314
	S	-1.595426	-0.651710	0.000000				593	596
	N	0.000000	0.836702	0.000000				1306	2169
	O	2.308460	0.193038	0.000000					
$\begin{array}{c} \text{S} - \text{C} \\ \quad \\ \text{O} - \text{N} \end{array}$	S	-1.106356	-0.430903	0.000000	-566.05986	0.01016	-566.04970	267	368
	O	1.143473	-0.651912	0.000000				613	720
	C	0.000000	1.054752	0.000000				809	1682
	N	1.221987	0.825889	0.000000					

	C	0.256401	0.021841	0.486672	-566.09830	0.00947	-566.08883	275	390
	S	-1.364114	0.000389	-0.073677				686	736
	N	1.369089	0.728024	-0.124271				794	1275
	O	1.337974	-0.654181	-0.108913					
COSN	C	-0.023854	-3.402638	0.000000	-566.14731	0.00699	-566.14033	17	28
	O	-0.050444	-2.275420	0.000000				42	46
	S	0.000000	1.143589	0.000000				718	2215
	N	0.078096	2.903110	0.000000					
CSNO	C	1.637985	0.709552	0.000000	-566.06128	0.00852	-566.05276	126	245
	N	-0.898887	-0.619877	0.000000				462	498
	S	0.000000	0.876229	0.000000				857	1552
	O	-0.441963	-1.742231	0.000000					
cis-SNCO	S	-1.401904	-0.034519	0.000000	-566.21350	0.01167	-566.20183	198	412
	O	1.816514	-0.766150	0.000000				654	827
	N	0.000000	0.687653	0.000000				1217	1813
	C	1.316390	0.311321	0.000000					
trans-SNCO	C	1.085191	-0.418881	0.000000	-566.20504	0.01106	-566.19397	172	202
	O	2.226855	-0.081848	0.000000				533	908
	N	0.000000	0.426373	0.000000				1247	1793
	S	-1.520374	0.011466	0.000000					

REFERENCE LIST

- Arrhenius, S. Z. *Physic. Chem.* **1889**, 4, 226.
- Becke, A. D. *J. Chem. Phys.* **1992**, 98, 1372.
- Benkhoff, J.; Boice, D. C. *Planet. Space Sci.* **1996**, 44, 665.
- Black, G.; Jusinski, L. E. *Chem. Phys. Letters* **1986**, 124, 90.
- Black, G.; Jusinski, L. E. *J. Chem. Phys.* **1985**, 82, 789.
- Bowman, J. M.; Zou, S. *Chem. Phys. Lett.* **2003**, 368, 421.
- Braun, W.; Lenzi, M. *Faraday Society* **1967**, 44, 252.
- Chase, M. W. *NIST JANAF Thermochemical Tables*, 4th ed.; American Institute of Physics: Woodbury, 1998.
- Cobos, C.; Troe, J. Z. *Phys. Chem.* **2003**, 217, 1031-1044.
- Dadong, X.; Jianhua, H.; Jackson, W. M. *J. Chem. Phys.* **2004**, 120, 3051.
- Dean, J. A., Ed. *Lange's Handbook of Chemistry*, 13th ed.; McGraw-Hill: New York, 1985.
- Dello Russo, N.; DiSanti, M. A.; Mumma, M. J.; Magee-Sauer, K.; Rettig, T. W. *Icarus* **1998**, 135, 377.
- Ding, L.; Marshall, P. *J. Chem. Soc. Faraday Trans.* **1993**, 89, 419-423.
- Evans, M. G.; Polanyi, M. *Trans. Faraday Soc.* **1936**, 32, 1333.
- Fenimore, C. P. *Symp. (Int.) Combust., [Proc.]*, 13th, Schenectady, NY, 1971; pp 373-380.
- Finlayson-Pitts, B. J.; Pitts, Jr., J. N. *Atmospheric Chemistry*; Wiley: Chichester, 1986.
- Fontijn, A.; Felder, W. *Reactive Intermediates in the Gas Phase*; Academic Press: New York, 1979.

Frisch, M. J.; Trucks, G. W.; Schlegel, H. B.; Scuseria, G. E.; Robb, M. A.; Cheeseman, J. R.; Montgomery, J. A. J.; Vreven, T.; Kudin, K. N.; Burant, J. C.; Millam, J. M.; Iyengar, S. S.; Tomasi, J.; Barone, V.; Mennucci, B.; Cossi, M.; Scalmani, G.; Rega, N.; Petersson, G. A.; Nakatsuji, H.; Hada, M.; Ehara, M.; Toyota, K.; Fukuda, R.; Hasegawa, J.; Ishida, M.; Nakajima, T.; Honda, Y.; Kitao, O.; Nakai, H.; Klene, M.; Li, X.; Knox, J. E.; Hratchian, H. P.; Cross, J. B.; Bakken, V.; Adamo, C.; Jaramillo, J.; Gomperts, R.; Stratmann, R. E.; Yazyev, O.; Austin, A. J.; Cammi, R.; Pomelli, C.; Ochterski, J. W.; Ayala, P. Y.; Morokuma, K.; Voth, G. A.; Salvado, P.; Dannenburg, J. J.; Zakrzewski, V. G.; Dapprich, S.; Daniels, A. D.; Strain, M. C.; Farkas, O.; Malick, D. K.; Rabuck, A. D.; Raghavachari, K.; Foresman, J. B.; Ortiz, J. V.; Cui, Q.; Baboul, A. G.; Clifford, S.; Cioslowski, J.; Stefanov, B. B.; Liu, G.; Liashenko, A.; Piskorz, P.; Komaromi, I.; Martin, R. L.; Fox, D. J.; Keith, T.; A, A.-L. M.; Peng, C. Y.; Nanayakkara, A.; Challacombe, M.; Gill, P. M. W.; Johnson, B.; Chen, W.; Wong, M. W.; Gonzalez, C.; Pople, J. A. Gaussian 03, revision C.02; Gaussian, Inc. Wallingford, CT, 2004.

Gargurevich, I. A. *Ind. Eng. Chem. Res.* **2005**, *44*, 7706.

Haubner, R.; Sommer, D. *Diamond Relat. Mater.* **2003**, *12*, 298.

Jeffries, J. B.; Crosley, D. R. *Combust. Flame* **1986**, *64*, 55.

Jensen, F. *Introduction to Computational Chemistry*; John Wiley & Sons: Chichester, 1999.

Krishnan, R.; Binkley, J. S.; Seeger, R.; Pople, J. A. *J. Chem. Phys.* **1980**, *72*, 650.

Lee, C.; Yang, W.; Parr, R. G. *Phys. Rev. A* **1989**, *37*, 78.

Leonori, F.; Petrucci, R.; Balucani, N.; Hickson, K.; Hamberg, M. *J. Phys. Chem. A* **2009**, *113*, 4330-4339.

Lindemann, F. A. *Trans. Faraday Soc.* **1922**, *17*, 598.

Little, D. J.; Donovan, R. J. *J. Photochem.* **1973**, *1*, 371-377.

Liu, K.; Han, W.; Pan, W.-P.; Riley, J. T. *J. Hazard. Mater.* **2001**, *B84*, 175.

Marshall, P. *Comput. Chem.* **1987**, *11*, 219.

Marshall, P. *Comput. Chem.* **1989**, *13*, 103.

Marshall, P. University of North Texas, Denton, TX. Personal Communication, 2013.

McGrath, W. D.; Morrow, T.; Dempster, D. N. *Chem. Commun.* **1967**, No. 11, 516.

Moolsradoo, N.; Watanabe, S. *Diamond Relat. Mater.* **2010**, *19*, 525.

Okabe, H. *Photochemistry of Small Molecules*; Wiley: New York, 1978.

Pilling, M. J.; Seakins, P. W. *Reaction Kinetics*; Oxford Science Publications: Oxford, 1995.

Pople, J. A.; Head-Gordon, M.; Raghavachari, K. *J. Chem. Phys.* **1987**, *87*, 5968.

Qu, Z.; Zhu, H.; Li, Z.; Zhang, X.; Zhang, Q. *Chem. Phys. Lett.* **2002**, *353*, 304.

Ristovski, Z. D.; Jayaratne, E. R.; Lim, M.; Ayoko, G. A.; Morawska, L. *Environ. Sci. Technol.* **2006**, *40*, 1314.

Seki, K.; Okabe, H. *J. Phys. Chem.* **1993**, *97*, 5284-5290.

Steinfeld, J. I.; Francisco, J. S.; Hase, W. L. *Chemical Kinetics and Dynamics*, 2nd ed.; Prentice Hall: Upper Saddle River, 1999.

Thompson, K. University of North Texas, Denton, TX. Personal Communication, 2013.

Troe, J. *J. Phys. Chem.* **1979**, *83*, 114.

van Roodselaar, A.; Safarik, I.; Strausz, O. P.; Gunning, H. E. *J. Amer. Chem. Soc.* **1978**, *100*, 4068-4073.

Watts, J. D.; Gauss, J.; Bartlett, R. J. *J. Chem. Phys.* **1993**, *98*, 8718.

Wendt, J. O. L.; Morcomb, J. T.; Corley, T. L. *17th Symp. (Int.) Combust.* **1979**, *17*, 671.

Wendt, J. O. L.; Wootan, E. C.; Corley, T. L. *Combust. Flame* **1984**, *58*, 144.

Woon, D. *J. Phys. Chem. A* **2007**, *111*, 11249-11253.

Xu, H.; Joens, J. *Geophys. Res. Lett.* **1993**, *20*, 1035.

Zeldovich, Y. B. *Doklady Akademii Nauk SSSR, Seriya A* **1946**, *51*, 217.

Ziehn, T.; Tomlin, A. S. *Int. J. Chem. Kinet.* **2008**, *40*, 742.